On the role of turbulence distortion on leading-edge noise reduction by means of porosity

Zamponi, R.; Satcunanathan, S.; Moreau, S.; Ragni, D.; Meinke, M.; Schröder, W.; Schram, C.

DOI
10.1016/j.jsv.2020.115561

Publication date
2020

Document Version
Final published version

Published in
Journal of Sound and Vibration

Journal of Sound and Vibration 485 (2020) 115561

Contents lists available at ScienceDirect

Journal of Sound and Vibration

journal homepage: www.elsevier.com/locate/jsvi

On the role of turbulence distortion on leading-edge noise reduction by means of porosity

R. Zamponi [a,*], S. Satcunanathan [b], S. Moreau [c], D. Ragni [d], M. Meinke [b], W. Schröder [b], C. Schram [a]

[a] von Karman Institute for Fluid Dynamics, Waterloosesteenweg 72, 1640 Sint-Genesius-Rode, Belgium
[b] RWTH Aachen University, Wüllnerstr. 5a, 52062 Aachen, Germany
[c] Université de Sherbrooke, Boul. de L'Université 2500, J1K 2R1 Sherbrooke, Québec, Canada
[d] Delft University of Technology, Kluyverweg 1, 2629 HS, Delft, the Netherlands

ARTICLE INFO

Article history:
Received 26 November 2019
Revised 26 June 2020
Accepted 30 June 2020
Available online 5 July 2020
Handling Editor: J. Astley

Keywords:
Turbulence-interaction noise
Porous materials
Rapid distortion theory
Rod-airfoil configuration

ABSTRACT

A possible strategy for the reduction of the aeroacoustic noise generated by turbulence interacting with a wing profile, also referred to as leading-edge noise, is represented by the implementation of a porous medium in the structure of the airfoil. However, the physical mechanisms involved in this noise mitigation technique remain unclear. The present work aims at elucidating these phenomena and particularly how the porosity affects the incoming turbulence characteristics in the immediate vicinity of the surface. A porous NACA-0024 profile equipped with melamine foam has been compared with a solid baseline, both airfoils being in turn subjected to the turbulence shed by an upstream circular rod. The mean wall-pressure distribution along the airfoils shows that the implementation of the porous material mostly preserves the integrity of the NACA-0024 profile's shape. Results of hot-wire anemometry and large-eddy simulations indicate that the porous design proposed in this study allows for a damping of the velocity fluctuations and it has a limited influence on the upstream mean flow field. Specifically, the upwash component of the root-mean-square of the velocity fluctuations turns out to be significantly attenuated in the porous case in contrast to the solid one, leading to a strong decrease of the turbulent kinetic energy in the stagnation region. Furthermore, the comparison between the power spectral densities of the incident turbulent velocities demonstrates that the porosity has an effect mainly on the low-frequency range of the turbulent velocity power spectrum. This evidence is in line with the results of the acoustic beamforming measurements, which exhibit a noise abatement in an analogous frequency range. On the basis of these observations, an interpretation of the phenomena occurring in the turbulence-interaction noise reduction due to a porous treatment of the airfoil is finally given with reference to the theoretical inputs of the Rapid Distortion Theory.

1. Introduction

The interaction between an airfoil and incident turbulence is an important source of aerodynamic noise in numerous applications that have a high societal impact, such as turbo engines [1,2], cooling systems for automotive and construction industries

* Corresponding author.
E-mail address: riccardo.zamponi@vki.ac.be (R. Zamponi).

https://doi.org/10.1016/j.jsv.2020.115561

[3,4] or high-lift devices on aircraft wings [5,6]. In these examples, the turbulence is generally produced by elements that are installed upstream of the airfoil and generate inflow distortions.

The turbulent eddies interacting with the leading edge are subjected to a rapid deformation that scatters part of their kinetic energy into sound [7]. A fundamental study on the noise emitted by this mechanism was performed by Amiet [8], who proposed a theory to predict the far-field acoustic power spectrum generated by an airfoil immersed in a turbulent flow. In this case, the spanwise correlation length and the integral length scale of the upwash turbulent velocity fluctuations constitute the key parameters for the prediction of the noise generated by the interaction with the incoming turbulence. Experimentally, the leading-edge noise generation process has been addressed by several authors. Paterson and Amiet [9] measured the emitted far-field noise and the unsteady surface pressure field of a NACA-0012 profile that was installed downstream of a turbulence grid and concluded that the prediction of incident turbulence-interaction noise can be carried out if the inflow properties are sufficiently documented. Olsen and Wagner [10] analysed the broadband noise generated by the impingement of turbulence on airfoils characterised by different shapes and observed that an increasing thickness corresponded to a reduced turbulence-interaction noise. Similar conclusions were drawn by Oerlemans and Migliore [11], who performed wind tunnel tests for six different airfoils at several angles of attack in a grid-generated turbulent flow. Moreau et al. [12] investigated the effect of the angle of attack and the airfoil shape by studying the noise emitted by three different mock-ups (a flat plate, a thin Controlled-Diffusion (CD) airfoil, and a thick NACA-0012 profile) interacting with a turbulent flow in a grid-airfoil configuration. The results of the experiments confirmed the previously mentioned thickness effect, whereas the impact of the angle of attack and the camber was found to be limited. Devenport et al. [13] also confirmed the influence of the effects of these parameters by testing three airfoils in a wind tunnel that was equipped with a turbulence grid. Additional numerical investigations on this influence were also carried out by Gill et al. [14] and Kim et al. [15].

The effective distortion of the turbulent vortical structures at the leading edge must be taken into account in order to obtain an accurate prediction of the leading-edge noise when the airfoil exceeds a minimum thickness [12,16,17]. In this regard, a useful analytical tool that can be considered for estimating the turbulence distortion around an airfoil with a significant thickness is the Rapid Distortion Theory (RDT), formulated by Hunt [18] and based on the work of Batchelor and Proudman [19]. This theory assumes a particular distortion to occur rapidly enough to have a negligible contribution from the turbulence to the relative motion of the fluid particles when these are convected through the non-uniform mean flow region. In addition, the turbulent velocity fluctuations are supposed to be small compared with the free-stream velocity. Recently, experimental evidence of the turbulence properties alteration that is predicted by the RDT for the case of a relatively thick airfoil was provided by De Santana et al. [17].

Since acting on the turbulence intensity of the incident flow is typically unfeasible, one possible leading-edge noise mitigation strategy is to make the airfoil less affected by local disturbances. The usage of absorbing materials, e.g. porous media, as part of the airfoil structure has the potential of achieving such a goal, as firstly demonstrated by Lee [20], who numerically investigated the effect that a porous leading-edge insert of a helicopter blade had on the turbulence-interaction noise. He observed that a far-field noise reduction of up to 30 % was possible due to the suppression of the pressure fluctuations at the blade surface.

Several researchers have already proposed technological solutions for the implementation of porous materials in the design of a wing profile in the last two decades. Among them, Roger et al. [7,21] filled a NACA-0012 profile with steel wool to study the leading-edge noise reduction from a grid-airfoil and rod-airfoil interaction. They found that a reduction ranging from 2.5 dB to 6 dB was achievable for a part of the spectrum that was related to the characteristic length of the porous medium. Likewise, Geyer et al. [22,23] manufactured numerous porous airfoils characterised by different materials and tested them with various grid-generated turbulent flows by means of microphone array techniques. They also focused their attention on the influence of the parameters characterising the porous media, observing how the noise reduction performance was strongly related to the material properties. Particularly, they found that lower values of static air flow resistivity could lead to a more significant noise reduction. Moreover, Sarradj and Geyer [24] investigated the leading-edge noise generation occurring at porous airfoils by symbolic regression tools and observed a dependency of the noise to the square of the turbulence intensity and from the fifth to sixth power of the flow velocity. The ratio of the integral length scale of the incoming turbulent flow to the characteristic length of the porous structure (linked to the static air flow resistivity) was found to have a significant influence on the noise frequency spectrum. Additional research on the application of a porous treatment of the airfoil was performed by Geyer et al. [25], who experimentally and numerically tested the effectiveness of perforated leading-edge inserts for the attenuation of grid-generated turbulence-interaction noise. A noticeable mitigation up to 8 dB was achieved for frequencies ranging from 1 kHz to 4 kHz. A different design for a flow permeable leading-edge insert has been investigated by Avallone et al. [26] and Sinnige et al. [27] for the suppression of the noise produced by the interaction of a pylon with a propeller slipstream. In this case, an attenuation of the tonal components of the emitted far-field noise was measured.

All these studies demonstrated the potential of a porous treatment of the airfoil as a turbulence-interaction noise reduction technique. However, no definitive explanation about the physical mechanisms involved in the noise mitigation has been found yet. One possible mechanism is linked to the dissipation of the acoustic energy by the viscous and thermal losses occurring during the oscillatory fluid motion in the pores of the material [28]. A second one is related to the hydrodynamic absorption of the turbulent eddies due to the interaction with a penetrable surface. As a consequence of this, the distortion experienced by the turbulence in the immediate vicinity of the airfoil may be affected by the porous treatment. The present research has the purpose of exploring the latter mechanism and builds upon the questions that have arisen in a previous piece of work where the noise mitigation performance of a porous wing profile was assessed by comparing with a solid baseline [29]. An airfoil design in which melamine foam was implemented as part of the structure of a NACA-0024 profile has been proposed by the authors in

that instance. The characterisation of the boundary layers around the two airfoil configurations showed the significant influence of the porosity on the flow field and the acoustic far-field measurements demonstrated the effectiveness of the treatment. In addition, Large-Eddy Simulations (LES) for the same experimental setup have been performed by Satcunanathan et al. [30] to predict the noise mitigation. Nonetheless, in both studies no analysis of the turbulence distortion was carried out and no conclusions could be drawn on the noise reduction mechanisms.

The above-mentioned issues have been addressed in this paper, which expands on the results previously obtained [29,30] and focuses on the analysis of the porosity effects on the turbulence distortion. Further experiments have been carried out to better investigate this aspect, whose interpretation constitutes the true added value of the present research. This measurement campaign has been conducted in the JAFAR facility of the von Karman Institute for Fluid Dynamics (VKI). The solid and porous cases have been compared considering a zero-lift angle of attack and a jet outlet flow speed of 30 ms^{-1}. The incident turbulence has been generated by placing a cylindrical rod upstream of the airfoil. In this arrangement, firstly proposed by Jacob et al. [31] as an aeroacoustic benchmark problem, the airfoil undergoes a broadband perturbation dominated by a shedding frequency, similarly to landing-gear applications [32]. The experimental investigation presented in the paper involves the measurement of the far-field noise with a phased-microphone array, the study of the mean wall-pressure distribution on the surface of the airfoils, and the characterisation of the mean and unsteady flow field in the stagnation region using a single-sensor hot-wire probe. The simulations provide complementary information about the description of the different turbulent velocity components and are employed to explain the experimental trends. Lastly, the power spectra of the velocity fluctuations measured by the hot-wire are computed in order to analyse whether they can be linked to the acoustic power spectra. Also in this case, the experiments are supplemented by the numerical results of the LES.

The paper is structured as follows: the experimental setup and the numerical formulation are presented in Section 2. Section 3 describes the experimental and numerical results, highlighting the turbulence distortion effects in the stagnation region, whereas in Section 4 the results are discussed considering the analytical inputs of the RDT. Finally, conclusions are drawn in Section 5.

2. Materials and methods

2.1. Rod-airfoil configuration

Fig. 1 shows a scheme of the rod-airfoil configuration installed in the JAFAR facility of VKI. A circular-to-rectangular contraction designed by De Santanta [33] adapts the circular geometry of the upstream duct to the rectangular geometry of the exhaust nozzle. The area ratio is 2.35 to 1 and the nozzle exit has a span of $s = 0.200$ m and a width of $l = 0.150$ m. Two side plates guide the flow and support the $d = 0.020$ m diameter cylindrical rod and the NACA-0024 profile, separated from each other by a distance of 0.174 m ($x/d = 8.20$). The airfoil chord is $c = 0.157$ m ($c/d = 7.85$) and the maximum thickness is approximately $t = 0.038$ m ($t/d = 1.90$). This value has been designed in order to have the same radius for the airfoil leading edge and the rod.

Given the relatively low aspect ratio $s/c = 1.27$ of the airfoil, some precautions were taken to minimise the risk of contamination of the acoustic field by corner effects. Firstly, the junctions between the airfoil and the holding side plates have been filled with a rounded fillet of plasticine (also to avoid any gap noise) with radius approximately equal to 0.003 m. This is known to reduce or even suppress the appearance of horseshoe vortices [34], which may otherwise produce noise when scattered at the trailing edge. Secondly, the thickness of the incoming boundary layer over the side plates is less than 0.002 m and is

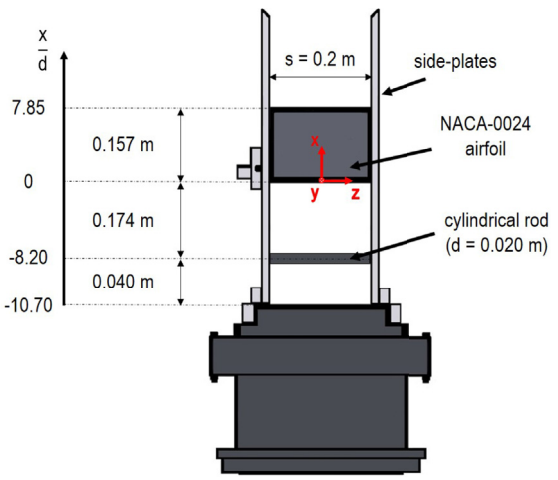

Fig. 1. Sketch of the rod-airfoil configuration installed in the JAFAR facility of VKI. The red arrows denote the coordinate axes of the reference system. (For interpretation of the references to colour in this figure legend, the reader is referred to the Web version of this article.)

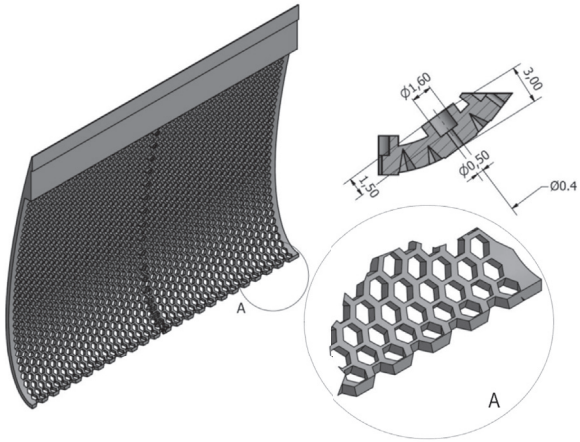

Fig. 2. Structure of the permeable exoskeleton exhibiting the hexagonal openings and the static pressure port.

characterised by a turbulence intensity well below that of the incoming turbulence in the main stream.

The following reference system, indicated by the red arrows in Fig. 1, has been adopted for the presentation of the results: the x-axis is aligned with the flow direction, the z-axis is aligned with the spanwise direction of the airfoil, and the y-axis is oriented in the normal direction in order to form a right-handed coordinate system. The origin is set at the midspan and at the leading edge of the airfoil mock-up.

2.2. Design of the airfoils

The same manufacturing technique has been used to design the solid and the porous versions of the airfoil. For both of them, a hard plastic exoskeleton with a thickness of 0.002 m preserves the structural integrity of the model. This is made of two components, one per each side of the airfoil surface, which have been glued together at the leading edge and the trailing edge. The porous airfoil exoskeleton features hexagonal openings throughout its surface, with a side-to-side length of 0.004 m and an equivalent open area ratio of 80 % to allow for the penetration of the air flow into the inner region. Fig. 2 illustrates a schematic of this component. The volume of the airfoil has been filled with melamine foam. A hard plastic impenetrable center-plane avoids the cross-flow between the two sides of the wing profile. However, its extent does not cover the first 6.4 % of the chord (one leading-edge radius) to allow for the penetration of the air flow at the stagnation point. Moreover, both airfoils have been coated with the same metallic woven wire mesh, which protects the materials and guarantees an adequate quality surface roughness. This is characterised by an aperture of 0.198 mm, a wire diameter of 0.056 mm, and an open area ratio of 60.8 %. Fig. 3(a) provides a sketch of the different parts of the porous airfoil, whereas a picture of the two manufactured prototypes is shown in Fig. 3(b).

Finally, the solid and the porous airfoils have been equipped with 35 static pressure sensors distributed along both sides of the airfoils, at corresponding streamwise locations (Fig. 3(a)). The transducers have been placed at the corners of the hexagonal openings in the midspan of the exoskeleton, thereby minimising the alterations of the local open area ratio, as shown in Fig. 2. The x-coordinates of the sensors range from 1 % to almost 80 % of the chord. Furthermore, an additional measurement position has been designed at the airfoil leading edge in order to acquire the stagnation pressure. The ports have then been connected to an in-house acquisition system for the evaluation of the mean wall-pressure distributions and the data have been acquired at a sampling frequency of 500 Hz, with an acquisition time of 15 s.

2.3. Characterisation of the porous medium

According to the Johnson-Champoux-Allard-Lafarge (JCAL) model [35–37], the six parameters that are necessary to fully characterise the porous material are the static air flow resistivity, σ, the porosity, φ, the tortuosity, α_∞, the viscous characteristic length, Λ, the thermal characteristic length, Λ', and the static thermal permeability, k'. Besides these, another property used to define a porous medium is the static viscous permeability, k, which is directly linked to σ by the relationship $k = \mu/\sigma$, μ being the dynamic viscosity of air.

The characterisation of the melamine foam parameters has been carried out in collaboration with the Laboratoire d'Acoustique de l'Université du Maine (LAUM). An inverse method based on the measurement of the scattering matrix by means of a 4-microphone impedance tube has been adopted [38]. The results are listed in Table 1. Furthermore, additional measurements have been performed at Centre de Transfert de Technologie du Mans (CTTM) using samples of the exoskeleton and the

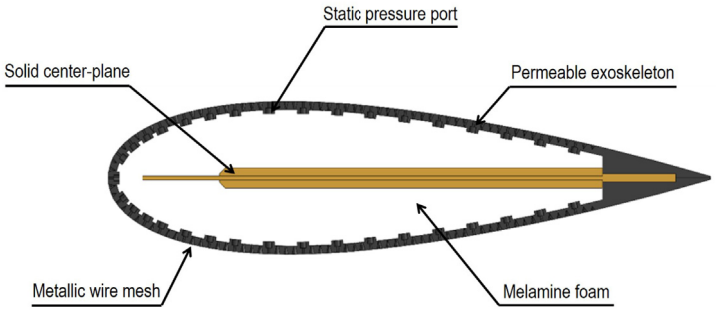

(a)

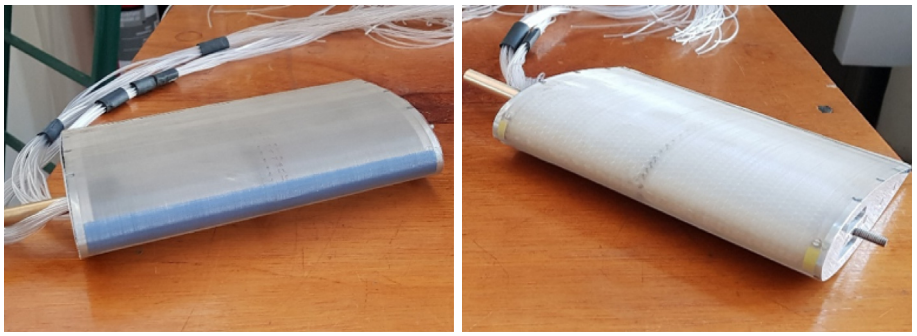

(b) (c)

Fig. 3. (a) Representation of the porous NACA-0024 profile featuring the solid center-plane, the hard-plastic exoskeleton, the metallic wire mesh and the static pressure ports. (b)–(c) Pictures of the solid airfoil (on the left) and the porous airfoil (on the right) manufactured at VKI.

Table 1
JCAL model parameters characterising the melamine foam of the porous airfoil.

σ [Pasm^{-2}]	φ [−]	α_∞ [−]	Λ [m]	Λ' [m]	k' [m^2]
8.683×10^3	0.986	1.02	1.344×10^{-4}	1.942×10^{-4}	2.305×10^{-9}

wire mesh. The static air flow resistivity of the two layers has been found to be negligible compared with that of the melamine foam.

All the measured parameters are provided to give a complete overview, but only part of them are necessary to model the porous airfoil in the LES, as will be covered in greater detail in Section 2.7.

2.4. Nozzle flow qualification

The experiments have been carried out at a free-stream flow velocity of $U_\infty = 30$ ms^{-1} that corresponds to a Reynolds number based on the rod diameter of $Re_d = 4.1 \times 10^4$. The airfoil is set at zero angle of attack, which has been verified by the mean wall-pressure distribution.

Profiles of the mean streamwise velocity, $\overline{U}$, and of the root-mean-square (r.m.s.) of the streamwise velocity fluctuations, U', have been obtained at the nozzle exit with a single hot-wire L-shaped probe. This has been connected to an in-house anemometer and installed in a carriage system, depicted in Fig. 4, that enables the automatic movement of the sensor within the yz plane. The static calibration of the hot-wire has been performed in-situ on a daily basis, using a Prandtl tube to measure the reference velocity. All the measurements have been corrected in order to take into account the temperature variations during the tests by following the method proposed by Bruun [39]. The sampling frequency has been set to 51.2 kHz, which has led to an anti-aliasing filter set to 25.6 kHz, and the data have been acquired for a duration of 5 s to keep the maximum relative uncertainty below 0.4 % for the mean velocity in the potential core of the jet.

Fig. 5(a) and (b) present the dimensionless mean velocity, $\overline{U}/U_\infty$, and the turbulence intensity, U'/U_∞, along the y-axis at $z = 0$ respectively. The probe has been placed 0.001 m downstream of the nozzle exit in the streamwise direction, corresponding to $x/d = -10.65$. The cylindrical rod has been removed to allow for the movement of the sensor. The mean velocity remains within 4 % of U_∞ across the potential core of the jet, whereas an increase of up to 9 % of U_∞ can be observed in proximity to the

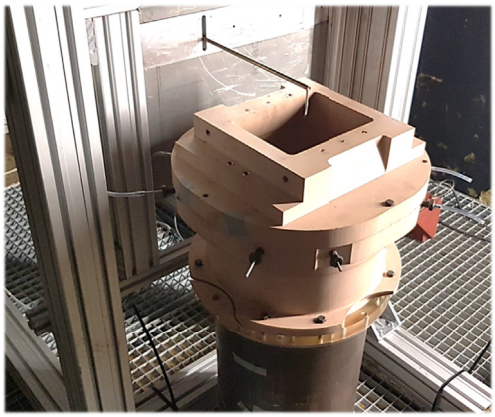

Fig. 4. Carriage system installed in the JAFAR facility for the automatic movement of the hot-wire L-shaped probe within the *yz* plane for the qualification of the facility.

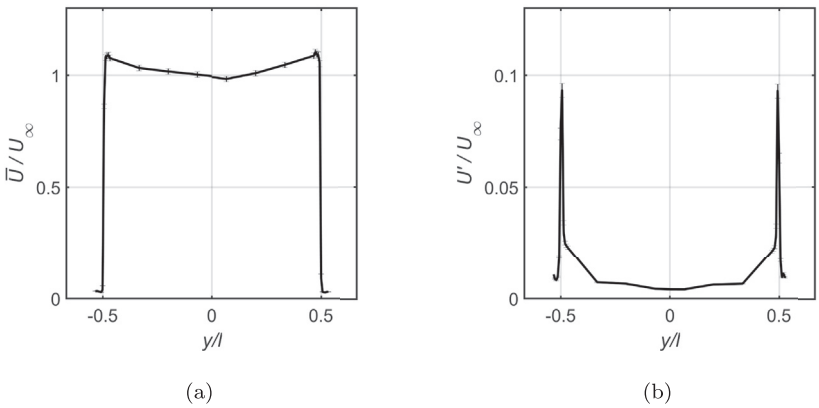

Fig. 5. Mean velocity (a) and turbulence intensity (b) profiles at $x/d = -10.65$, corresponding to $x = -0.213$ m, at the airfoil midspan.

nozzle edges. The sharp transition in the velocity between the potential core and the no-flow region indicates a limited width for the shear layer, as would be expected at such a short distance from the nozzle exit. In Fig. 5(b), the turbulence intensity is found to be about 0.4 % in the potential core of the jet. Finally, the peaks in turbulence intensity are located in the two shear layer regions and amount to almost 10 %, with an uncertainty below 1.4 %. The present results have been used as boundary conditions for the numerical prediction of the flow field, as reported in Section 2.7.

2.5. Flow field characterisation

The investigation of the stagnation region surrounding the airfoil leading edge has been conducted using the same hot-wire anemometer employed for the nozzle flow qualification. In this case, the carriage system has been rotated in order to enable the movement of the probe along the *x*-direction. The wire has been mounted on a straight probe oriented perpendicularly to the flow direction. The sampling frequency has been set to 51.2 kHz, whereas the acquisition time has been extended to 10 s in order to ensure statistical convergence in the computation of the velocity power spectral density (PSD) of the incident velocity fluctuations. This quantity has been processed by means of the Welch method [40], with blocks of 2^{13} samples windowed using a Hanning weighting function that is characterised by a 50 % data overlap, thus providing a frequency resolution of 6.25 Hz. The same parameters have been employed to compute the PSD from the LES data. Furthermore, the temperature variations have been corrected by following the model proposed by Bruun [39].

Fig. 6 illustrates the measurement positions of the single traverse acquired along the stagnation streamline. The *x*-coordinate is normalised by the leading-edge radius, r_{LE}. The traverse has been designed at $z = 0.1\,s$ in order to avoid the influence of the static pressure port on the measurement points close to the airfoil surface. 55 locations have been considered, with the probe moving in the streamwise direction from the upstream flow region towards the airfoil leading edge. The distance between consecutive measurement positions varies from 2.0 mm, to 1.0 mm, and finally to 0.5 mm as shown in Fig. 6. The minimum distance of the probe from the surface less than 0.5 mm has been evaluated using a dummy sensor having the same geometry as

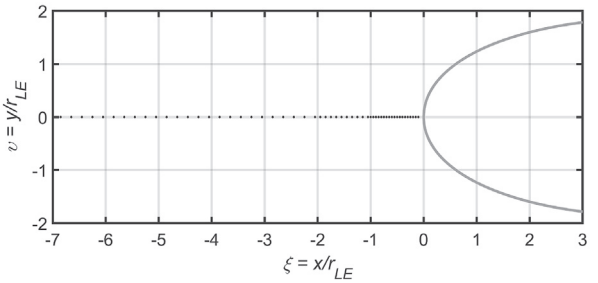

Fig. 6. Traverse designed for the characterisation of the stagnation streamline by means of hot-wire anemometry consisting of 55 points at $z = 0.1$ *s*. The distance between the points is 2.0 mm, 1.0 mm, and 0.5 mm for respectively the first 50 mm (5 r_{LE}), the following 10 mm (1 r_{LE}), and the final 10 mm (1 r_{LE}) of the traverse, whereas the minimum distance of the probe from the surface is 0.5 mm.

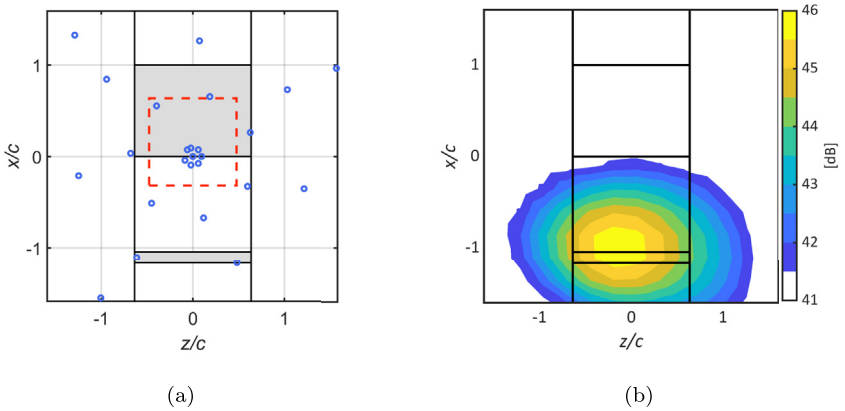

Fig. 7. (a) Configuration of the GIBF sound map, with the black lines indicating side-plates, rod, and airfoil leading edge and trailing edge, the red dashed lines denoting the source integration area, and the blue dots illustrating the projection of the central microphones positions on the scanning grid plane. (b) GIBF sound map for the solid airfoil at $f_{1/3} = 250$ Hz computed with a reference pressure $p_{ref} = 20$ μPa. No background noise removal has been applied. (For interpretation of the references to colour in this figure legend, the reader is referred to the Web version of this article.)

the hot-wire probe. In this way, it has been possible to optically determine the exact position at which the prongs of the sensor touch the surface of the airfoil at the leading edge without harming the actual probe.

2.6. Acoustic beamforming setup

The noise reduction performance that is achieved with a porous treatment of the airfoil has been evaluated by means of acoustic beamforming. A seven arms Dougherty array [41] has been used for the measurements. This has been placed at 1.160 m from the airfoil, out of the flow, and its center has been approximately aligned with the midspan of the airfoil leading edge. The array has an aperture of 1.500 m and is equipped with 64 capacitor-based Knowles electret microphones model FG-23329-P07 (frequency response: ±3 dB; frequency range: from 100 Hz to 10 kHz), calibrated in amplitude and in phase. Fig. 7(a) depicts the projection of the central microphones positions on the scanning grid plane. The data have been acquired at a sampling frequency of 51.2 kHz for 60 s. The cross-spectral matrix of the measured signals has been computed by employing the Welch method [40], with blocks of 2^{13} samples windowed using a Hanning weighting function that is characterised by a 50 % data overlap, thus providing a frequency resolution of 6.25 Hz.

The acoustic data have been post-processed using a Generalized Inverse Beamforming (GIBF) technique developed at VKI and validated with both numerical and experimental benchmark datasets [42–45]. Corrections to account for the convection of the flow and the refraction of the shear layer have been applied by following the method proposed by Sijtsma [46]. The use of an advanced beamforming algorithm turns out to be crucial to properly isolate the different noise source contributions coming from the open jet, the rod self-noise, and the noise sources generated at the juncture of the side-plates and the airfoil due to the scattering of the turbulent boundary layer forming along the plates. Particularly, the rod-noise has been found to be the dominant source for a major part of the sound frequency spectrum, making it difficult to measure the leading-edge noise produced by the airfoil with a single microphone. This is a consequence of the thickness effect of the NACA-0024 profile that decreases the efficiency of the noise generation mechanism, as mentioned in Section 1.

A proper handling of the background noise is also required to ensure a better evaluation of the sound maps. Hence, the advanced subtraction technique developed by Bahr and Horne [47] has been employed. In this case, the acquired background noise corresponds to a configuration where the airfoil has been removed. Indeed, the distance between the rod and the airfoil is such that the vortex shedding is not suppressed by the presence of the body and the vortex-shedding frequency remains unaltered, making it feasible to perform the subtraction. An example of a GIBF sound map where no background noise removal has been applied is reported in Fig. 7(b). The map refers to the solid airfoil and has been computed at the one-third octave band center frequency $f_{1/3} = 250$ Hz and with a reference pressure of $p_{\text{ref}} = 20$ μPa.

Moreover, GIBF is based on the eigendecomposition of the cross-spectral matrix of the microphone signals and each eigenvalue is linked to a coherent source distribution under constraint of orthogonality [48]. This feature makes it possible to select a subset of eigenmodes to process, which corresponds only to the actual sources of interest, such as the ones generated by turbulence-interaction. A similar approach has been followed by Zamponi et al. [49] for characterising the aeroacoustic noise sources of a counter-rotating open rotor by means of GIBF. In the present investigation, one eigenmode has been found to be dominant for each frequency after the background subtraction and, therefore, has been computed by the algorithm.

An extensive analysis of the acoustic beamforming sound maps has been already reported in Zamponi et al. [29]. In that instance, the investigation was limited to the one-third octave band center frequencies ranging from 1 kHz to 5 kHz and a significant noise increase was observed starting from 2 kHz. The origin of this phenomenon can be attributed to the presence of the exoskeleton that induces a cross-flow within its hexagonal pores and alters the surface roughness. This hypothesis is supported by the agreement between the results of the boundary layer characterisation and the ones of similar studies conducted on porous surfaces [25,26,50].

The focus of the present analysis is on the low-frequency range in order to investigate the noise reduction around the vortex shedding frequency. At low frequencies, the resolution of the beamforming sound maps is typically too low to exhibit a clear representation of the distributed noise sources along the leading edge due to the beamwidth characteristics of the microphone array. Nevertheless, the information on the source strength is preserved and it can be evaluated by integrating the sound maps after their decontamination from the background noise. The integration is then performed by summing the pressure values of each scanning grid point within a square region surrounding the airfoil leading edge.

A sketch of the experimental setup to yield the sound maps is illustrated in Fig. 7(a). The scanning grid ranges between $-2 < z/c < 2$ and $-2 < x/c < 2$, with a spatial resolution of 0.010 m. The vertical black lines indicate the test section side-walls, the cylindrical rod, the leading edge, and the trailing edge of the airfoil. The red dashed lines indicate the considered integration area, which is located within the potential core of the jet and has a dimension of 0.15 m × 0.15 m.

2.7. Numerical simulations

This section provides a brief summary of the LES method and the porous model, the details of which have been given in Satcunanathan et al. [30]. Statistics and spectra of both streamwise and upwash turbulent velocity components have been extracted from the numerical simulations in order to complement and interpret the experimental data of the single hot-wire anemometer.

Within the LES, the air-saturated porous medium is treated by the method of volume-averaging [51] applied to the conservation equations of mass, momentum, and energy. The flow inside the porous medium is equally defined in the fluid and the solid phase by the spatially filtered continuously varying field variables in space and time. Using $\langle\rangle$ to denote the intrinsic average and $\langle\rangle_F$ the Favre average, the compressible volume averaged Navier-Stokes (VANS) equations in non-dimensional strong form read

$$\frac{\partial \widehat{\mathbf{Q}}}{\partial t} + \nabla \cdot \left(\widehat{\mathbf{H}}^{inv} - \widehat{\mathbf{H}}^{vis} \right) + \frac{1}{\varphi} \widehat{\mathbf{H}}^{int} \cdot \nabla \varphi + \boldsymbol{\mathcal{S}} = 0, \tag{1}$$

$\widehat{\mathbf{Q}} = \left[\langle\rho\rangle, \langle\rho\rangle\langle\mathbf{u}\rangle_F, \langle\rho\rangle\langle E\rangle_F \right]^T$ being the vector of spatially averaged conservative variables. The inviscid and viscous flux tensors are given by

$$\widehat{\mathbf{H}}^{inv} - \widehat{\mathbf{H}}^{vis} = \begin{bmatrix} \langle\rho\rangle\langle\mathbf{u}\rangle_F \\ \langle\rho\rangle\langle\mathbf{u}\rangle_F \otimes \langle\mathbf{u}\rangle_F + \langle p\rangle\mathbf{I} \\ \langle\rho\rangle\langle E\rangle_F\langle\mathbf{u}\rangle_F + \langle p\rangle\langle\mathbf{u}\rangle_F \end{bmatrix} - \frac{1}{Re_d} \begin{bmatrix} 0 \\ \langle\boldsymbol{\tau}\rangle_F \\ \langle\boldsymbol{\tau}\rangle_F \cdot \langle\mathbf{u}\rangle_F + \frac{1}{Pr}\langle\mathbf{q}\rangle \end{bmatrix} \tag{2}$$

and the contribution of the inviscid flux vector at the fluid-porous interface is $\mathbf{H}^{int} = \mathbf{H}^{inv} - \langle p\rangle\mathbf{I}$. The quantities ρ, p, $\mathbf{u}$, E, $\boldsymbol{\tau}$, $\mathbf{q}$, $\mathbf{I}$, Re_d, and Pr denote the density, the pressure, the velocity vector, the total energy, the shear stress tensor, the heat flux vector, the unit tensor, the Reynolds number based on the rod diameter and the free-stream flow velocity, and the Prandtl number respectively. The surface filter term $\boldsymbol{\mathcal{S}} = \left[0, \boldsymbol{\mathcal{F}}/\varphi, 0\right]^T$ contains the porous drag $\boldsymbol{\mathcal{F}}$ that is closed by means of the Darcy-Forchheimer model, expressed for a homogeneous and isotropic porous medium by

$$\boldsymbol{\mathcal{F}} = \underbrace{\frac{1}{Re_k\sqrt{Da}}\varphi\mu\langle\mathbf{u}\rangle_F}_{Darcy} + \underbrace{\frac{1}{\sqrt{Da}}\varphi^2 c_F\langle\rho\rangle|\langle\mathbf{u}\rangle_F|\langle\mathbf{u}\rangle_F}_{Forchheimer}. \tag{3}$$

Table 2
Darcy-Forchheimer model parameters characterising the melamine foam for $L = d$.

φ [−]	Da [−]	c_F [−]	Re_k [−]
0.986	5.3×10^{-6}	0	92

The permeability Reynolds number, $Re_k = Re_d\sqrt{Da}$, is defined with $d_p\%\sqrt{k}$ as the length scale, which is a measure for the effective pore diameter, whereas the Darcy number, Da, is defined as $Da = k/L^2$, L being some reference length. The Darcy-Forchheimer model (Eq. (3)), together with Eq. (1), characterises the porous medium in terms of the porosity, φ, the permeability, k, and the Forchheimer coefficient, c_f, and assumes the porous frame to be rigid, neglecting coupling effects due to elasticity as well as thermal effects.

The material parameters from Section 2.3 that have been used to calibrate the Darcy-Forchheimer model are the porosity and static air flow resistivity. This can be also inferred from the JCAL model for $\omega \to 0$, which corresponds to the case of a directed flow through the porous material, as a limiting case of the acoustic wave behavior. The equivalent flow setup is that of a flow with a constant volume rate through the porous material, which then experiences a pressure drop. The calibration of the model parameters by a best fit to match the pressure drop of the real melamine foam of the experiments at one operating point prevented the simultaneous determination of k and c_F. Therefore, the latter was set to zero, which equates to omitting the quadratic Forchheimer contribution. The parameters are summarised in Table 2, where the permeability is given in terms of Da, with $L = d$. More details on the model calibration are provided in Satcunanathan et al. [52].

The equations are solved by a finite-volume method, which have been discretised in space by an advective upstream splitting method (AUSM) for the inviscid fluxes and a centered discretisation of the viscous fluxes. The semi-discretised equations are advanced in time by an explicit Runge-Kutta scheme. The overall scheme is second-order accurate in space and time. The LES is based on the monotone integrated LES (MILES) ansatz. The equations are discretised on a locally refined, unstructured, Cartesian mesh with a fully conservative cut-cell approach for the wall boundaries [53]. Details concerning the immersed boundary treatment of the fluid-porous interface are given in Satcunanathan et al. [30].

Two simulations have been set up, one for the solid and one for the porous airfoil. Both are supposed to match the experimental setups described in Section 2. For the porous airfoil, modelling the exoskeleton and the wire mesh as a homogeneous porous material is impractical for two reasons. On the one hand, it requires the specification of a porosity and a static air flow resistivity, which have been found to be negligible compared to that of the bulk volume. On the other hand, a scale separation between a representative averaging volume and the spatially averaged flow features of interest is not feasible and prevents the hexagonal openings from being treated as pores in the classical sense. The alternative of fully resolving the exoskeleton and the wire mesh has been omitted here for reasons of efficiency. Consequently, surface roughness effects are not captured. To maintain the shape of the airfoil and investigate the exclusive effect of the melamine foam, the dimensions of the porous airfoil are assumed to match the solid airfoil. The dominating qualitative effects are thus expected to result from the bulk melamine foam.

The computational domain extends $90\,d \times 64\,d \times \pi\,d$ in the streamwise, normal, and spanwise direction, resulting in 186 million mesh points for the baseline case and 206 million mesh points for the porous case. In the spanwise direction, periodic boundary conditions have been applied and synthetic eddies of uniform intensity have been superimposed to the inflow jet [54] at the inlet. After the transient, the flow field has been time-averaged and statistics of the turbulent flow field have been processed for a total of $T_s u_\infty/d = 161$ time units corresponding to approximately 32 shedding cycles at a Strouhal number of $St = 0.2$ to get converged statistics.

3. Results

In this section, the results of acoustic beamforming are first presented. Subsequently, the influence that the porous material has on the flow field around the solid and porous airfoil is analysed through mean wall-pressure distribution measurements. Finally, the outcomes of the experimental and numerical investigation of the flow field alterations within the stagnation region are discussed.

3.1. Aeroacoustic measurements

Fig. 8(a) and (b) show the GIBF sound maps for the solid and the porous airfoils respectively and refer to the one-third octave band center frequency $f_{1/3} = 250$ Hz, which corresponds to the band that includes the vortex shedding frequency. The maps provide the one-third octave band sound pressure level $L_{p(1/3)}$ calculated with a reference pressure of $p_{\text{ref}} = 20$ μPa and they are presented considering the same dynamic range of 10 dB. As already mentioned in Section 2.6, the noise source region does not appear distributed at the leading edge but extends over most of the airfoil surface for both solid and porous cases. Nevertheless, the adopted dynamic range allows for a visual estimation of the noise reduction achieved at this frequency range due to the porous treatment.

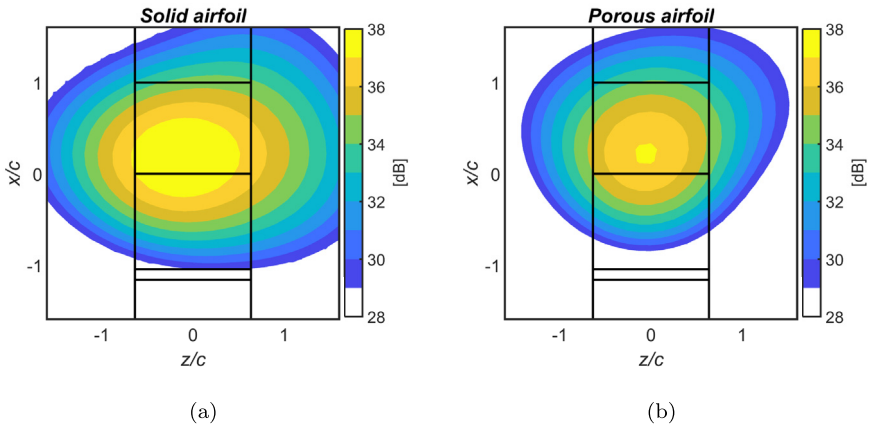

Fig. 8. GIBF sound maps exhibiting the noise source distribution contours for the solid (a) and porous (b) airfoil at $f_{1/3} = 250$ Hz. The maps are plotted with the same 10 dB dynamic range for both cases and computed with a reference pressure of $p_{\text{ref}} = 20$ µPa. A background subtraction technique is applied to reduce the rod-noise contribution.

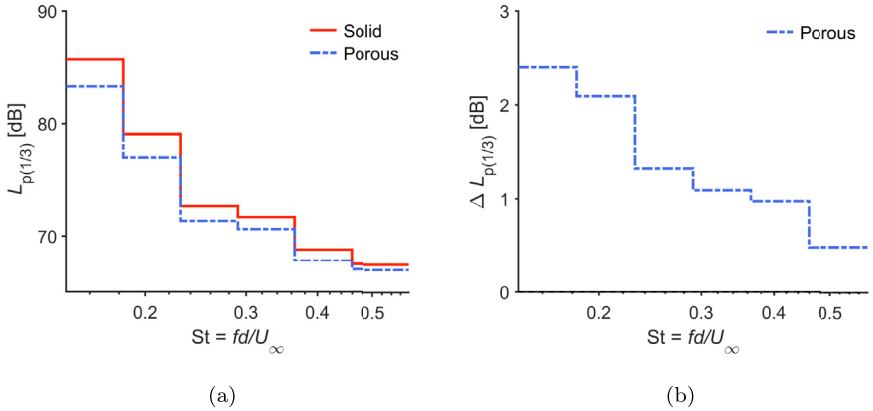

Fig. 9. (a) GIBF integrated one-third octave band spectra referred to the one-third octave band center frequencies ranging from 250 Hz to 800 Hz for the solid airfoil (red solid line) and the porous airfoil (blue dash-dotted line) and computed with a reference pressure of $p_{\text{ref}} = 20$ µPa. (b) Relative noise reduction due to the porous treatment of the airfoil with respect to the solid case. (For interpretation of the references to colour in this figure legend, the reader is referred to the Web version of this article.)

Furthermore, inverse beamforming methods such as GIBF display the source distribution contours instead of the peak source intensity, differently from direct techniques [48]. Hence, the integration of the maps is required to assess the actual noise source strength. This explains the relatively low levels of the sound maps in Fig. 8.

The resulting sound maps for one-third octave band center frequencies ranging from 250 Hz to 800 Hz have been subsequently integrated with reference to the center of the array. The integrated spectra for both airfoils are presented in Fig. 9(a), whereas the relative one-third octave band sound pressure level $\Delta L_{p(1/3)}$ of the porous airfoil with respect to the solid one is shown in Fig. 9(b) for a better representation of the noise reduction. The greatest abatement occurs at lower frequencies, in correspondence with the band containing the tonal component at the shedding frequency, and amounts to about 2.5 dB. For higher *St*, the noise mitigation gradually decreases and solid and porous spectra start converging.

However, the noise reduction performance achieved in the present work appears to be low if compared to the results of the investigations discussed in Section 1. This limited efficiency may be related to the presence of the exoskeleton that decreases the flow penetration into the melamine foam. Another possible explanation for the lower performance of the porous treatment is represented by the center-plane. Indeed, the acoustic waves generated on the airfoil surface can potentially penetrate the porous medium and interact with the solid walls of this component, similarly to the effect of the material junctions in the case of a porous leading-edge insert [55]. Further parametric studies will be performed in the near future to analyse the influence of the center-plane on the noise reduction.

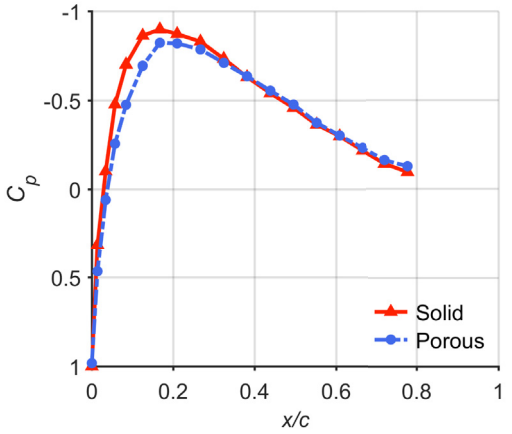

Fig. 10. C_p distribution along the airfoil chord measured for the solid (red solid line) and the porous (blue dash-dotted line) airfoil for $U_\infty = 30\ \mathrm{ms}^{-1}$ and for a 0° angle of attack. (For interpretation of the references to colour in this figure legend, the reader is referred to the Web version of this article.)

3.2. Mean wall-pressure distribution

The results of the mean wall-pressure distribution measurements are presented by defining the pressure coefficient C_p as

$$C_p = \frac{p - p_\infty}{p_{0,s} - p_\infty}, \tag{4}$$

where p is the measured mean wall-pressure and p_∞ and $p_{0,s}$ are respectively the static pressure in the free-stream and the stagnation pressure measured at the leading edge of the solid airfoil.

The C_p distributions along the chord for the solid and porous airfoils are shown in Fig. 10. Each point of the curve has been calculated by averaging the mean wall-pressure acquired on the two sides of the airfoil at the same chord position.

The alteration of the mean pressure field by the porous treatment appears to be mostly confined to the upstream 30 % of the airfoil, despite the fact that the melamine foam fills the porous airfoil up to 80 % of the chord. Nonetheless, the pressure recovery experienced by the solid NACA-0024 profile downstream of the maximum thickness is slightly higher than the one in the porous case, with a deviation that increases as the trailing edge is approached. The maximum difference at $x/c = 0.8$ is approximately $|\Delta C_p| = 0.03$. The present trend agrees with the thicker boundary layer that has been observed in the aft part of the porous airfoil in previous works [29,30]. Furthermore, the two configurations exhibit almost the same pressure at the stagnation point, although this value does not correspond to the free-stream dynamic pressure since the airfoil is immersed in the wake of the rod.

The negative C_p peak for the two airfoils occurs at 17 % of the chord and is almost preserved, being its absolute value reduced by 6.7 % in the porous case. Moreover, for the porous airfoil, this peak is reached in a more gradual way. The discrepancy can be explained by the partial penetration of the air flow through the pores of the melamine foam that tends to level out the pressure differences along the surface and reduces the flow displacement by the NACA-0024 profile. This would most likely degrade the lift of the airfoil if placed at some non-zero angle of attack, as reported in similar works [56,57].

3.3. Mean and fluctuating velocity field along the stagnation streamline

The experimental hot-wire data along the stagnation streamline presented in Section 2.5 are compared with the results of the LES presented in Section 2.7 by relating the statistics of the flow velocity field acquired by the single-probe hot-wire anemometer and the simulated ones. This comparison is meant to validate the numerical results that will be presented in the following section of the paper.

The quantities u, v, and w indicate the simulated velocity components in the x, y, and z direction and the symbols – and ′ denote the mean velocity and the r.m.s. of the velocity fluctuations respectively. Evaluating the magnitude of the two mean velocity components that are perpendicular to the wire in each sampling point, i.e., $\overline{u}$ and $\overline{v}$, $\overline{U}$ reads

$$\overline{U} = \sqrt{\overline{u}^2 + \overline{v}^2}. \tag{5}$$

Similarly, the formulation proposed in this paper to estimate U' is

$$U' = \sqrt{(u' \cos\alpha)^2 + (v' \sin\alpha)^2} \qquad \text{with} \quad \alpha = \tan^{-1}\left(\frac{\overline{v}}{\overline{u}}\right). \tag{6}$$

This quantity does not correspond to the r.m.s. of the velocity fluctuations that are given by the magnitude of the two velocity components measured by the probe, but rather represents a weighted average of u' and v' based on the local mean flow direction, which is expressed by the parameter α. This is a consequence of the fact that, for small turbulence levels, a single normal hot-wire only responds to fluctuations in the direction of the mean velocity [58].

Nonetheless, the proposed method to evaluate the local mean flow direction and therefore the contribution of the different velocity fluctuations components to U' could not be applicable if the numerical data were taken precisely on the stagnation streamline. Indeed, in such circumstances, $\overline{v}$ would be zero along the whole traverse and so would α due to the flow symmetry. Hence, U' would correspond to u' and no influence of v' would be detected. In order to tackle the problem, the LES data were extracted at $y = 8.8 \times 10^{-5}$ m. This distance was close enough to provide a negligible deviation from the flow field statistics computed on the stagnation streamline and far enough to have a non-zero value of $\overline{v}$ in the stagnation region.

The hot-wire anemometry results indicate that the implementation of the porous material in the airfoil structure preserves the potential effect with regard to the upstream flow. Fig. 11(a) illustrates the mean velocity profile along the stagnation streamline for the solid and the porous airfoils. $\overline{U}$ is normalised by the free-stream velocity. As can be observed, the experimental data for the two cases follow the same trend up to the immediate vicinity of the leading edge. This conclusion is supported also by the relatively small deviation in the solid and porous C_p distributions of Fig. 10.

Moreover, the hot-wire data are in a fairly good agreement with the numerical results corresponding to the solid airfoil for $\xi = x/r_{LE} \leq -1$. The deviation that is present for $\xi > -1$ has been already reported by Bearman [59] and is probably due to a thermal effect produced by the proximity to the surface or due to the intrusiveness of the hot-wire probe that has moved the stagnation point slightly. By contrast, the numerical results computed for the porous case do not follow the same trend as the solid one, hinting at an alteration of the airfoil's potential effect. The discrepancy may be linked to the absence of the hard-plastic

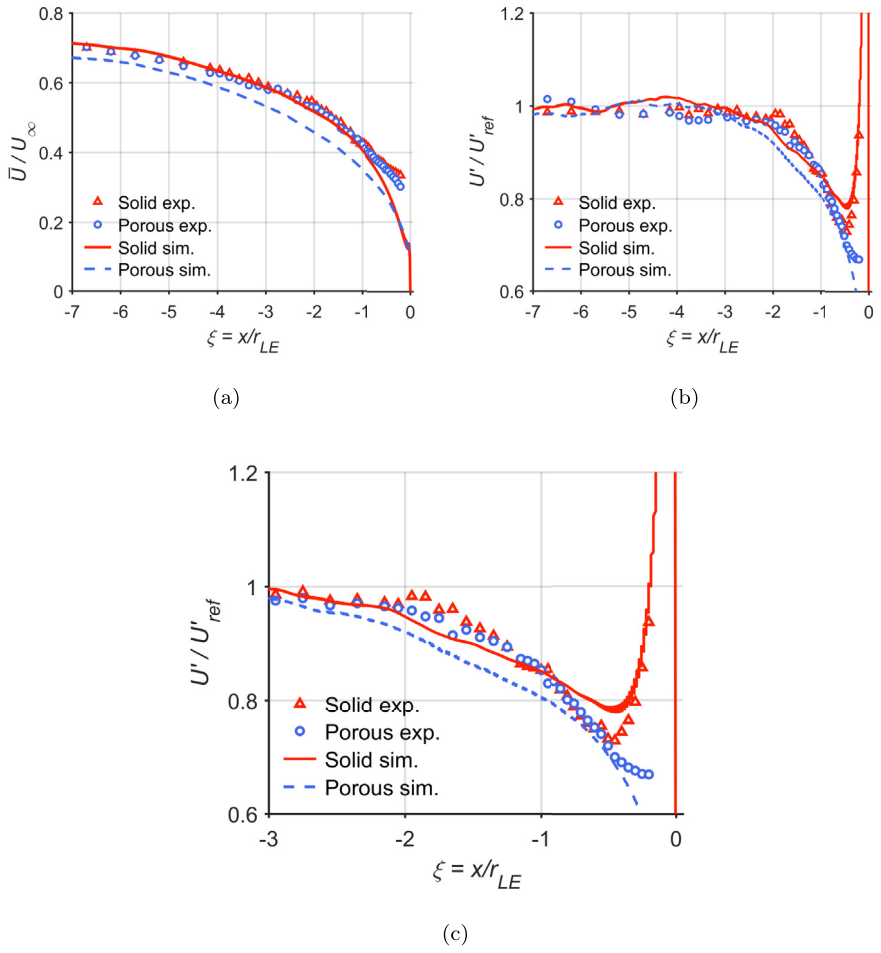

Fig. 11. Mean velocity profile (a) and velocity fluctuation profile (b)–(c) of the solid (in red) and porous (in blue) airfoil along the stagnation streamline for $U_\infty = 30$ ms^{-1} and for a 0° angle of attack. The solid and dash-dotted lines refer to the numerical results of the LES, whereas the triangle and dot symbols refer to the VKI experimental data. U'_{ref} corresponds to the r.m.s. of the velocity fluctuations evaluated at $\xi = -7$ for the solid case. (For interpretation of the references to colour in this figure legend, the reader is referred to the Web version of this article.)

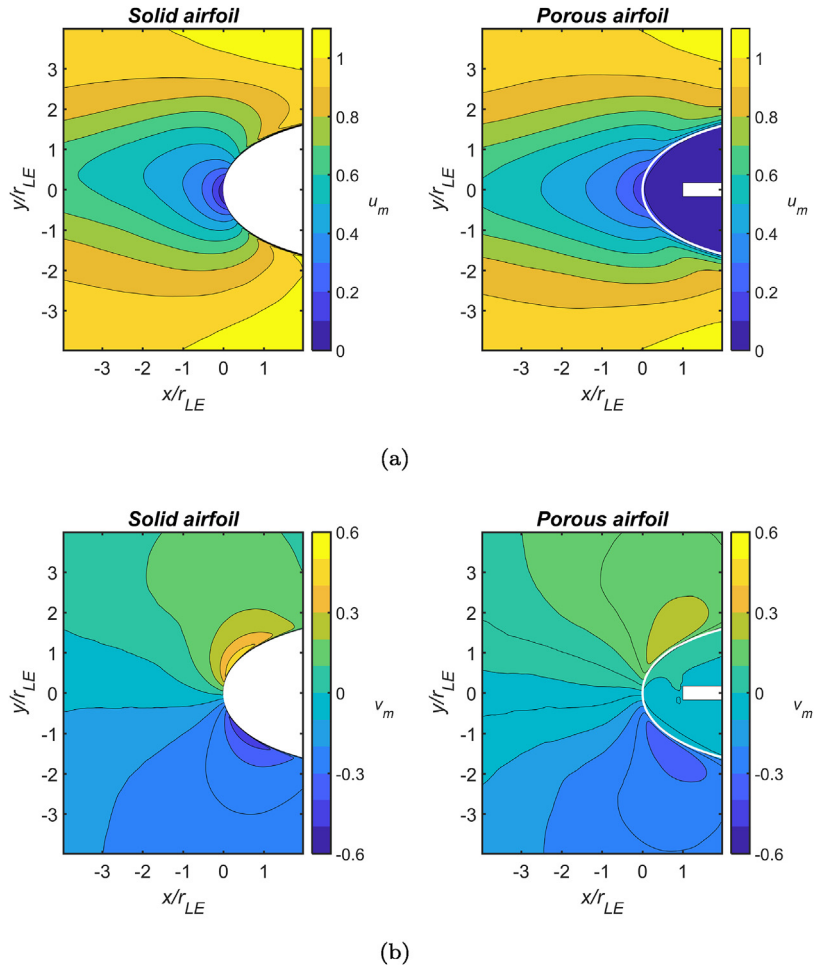

Fig. 12. Mean velocity for the solid (on the left) and the porous airfoil (on the right) in the stagnation region extracted by the LES. The $\overline{u}$- (a) and the $\overline{v}$-component (b) are made dimensionless by the free-stream velocity, U_∞.

permeable exoskeleton and the wire mesh in the numerical model of the porous medium, as explained in Section 2.7.

The most striking effect of porosity is on the evolution of the turbulent velocity fluctuations in the immediate vicinity of the leading edge. The velocity fluctuation profile along the stagnation streamline for the solid and the porous airfoil is depicted in Fig. 11(b) and an enlargement of the same plot is reported in Fig. 11(c). The velocity U' is normalised with an upstream reference value, U'_{ref}, which corresponds to the r.m.s. of the velocity fluctuations that has not been affected by the presence of the airfoil yet. This notation is consistent with the one by Batchelor and Proudman [19], Bearman [59], Hunt [18], and Britter et al. [60] in their investigations of the turbulence distortion. U'_{ref} has been evaluated at $\xi = -7$ and refers to the solid case. As can be seen from the plot, the experimental data present a similar trend up to about 0.5 r_{LE} from the leading edge, with a constant value equal to 1 for $\xi < -2$ and a decrease in the region $-2 \leq \xi < -0.5$. After this threshold, the solid and the porous cases diverge significantly, the former starts to increase and the latter keeps decreasing.

Furthermore, a good agreement is found between the numerical and the experimental data for both solid and porous airfoils in this case, indicating that the previously mentioned thermal effects do not affect the measurement of the velocity fluctuations performed by the hot-wire. Notably, the slope with which U' increases in the immediate vicinity of the solid airfoil is well predicted by the simulations, although a slight underestimation is observed for the minimum peak at $\xi = -0.5$. However, for the porous case, a small discrepancy is visible for $\xi > -0.5$. Analogously to the mean velocity comparison, this may be associated with the fact that the exoskeleton and the wire mesh have not been modelled in the numerical simulations.

3.4. Mean and fluctuating velocity in the stagnation region

Mean and r.m.s. velocities have been extracted from the LES to analyse the velocity components independently and to explain the hot-wire trends in Fig. 11. Fig. 12(a) and (b) present the mean velocity in the stagnation region for the solid and the porous cases. As indicated by the white airfoil outline, the LES provide an estimation of the flow field partially penetrating into the

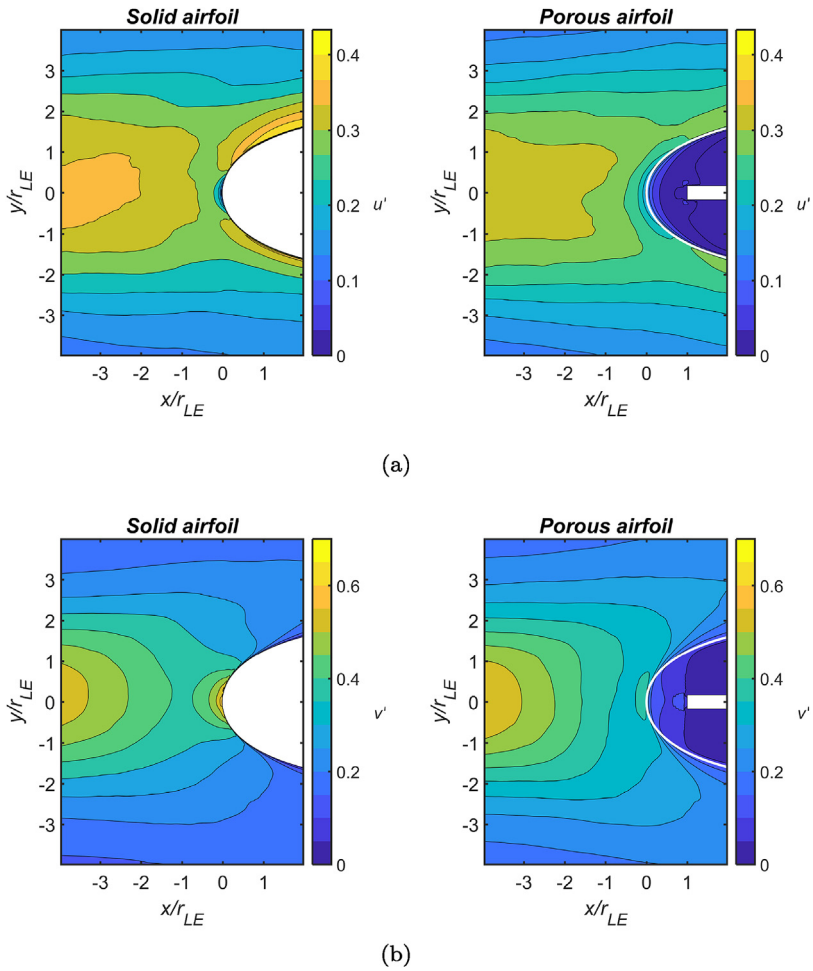

Fig. 13. Turbulence intensity for the solid (on the left) and the porous airfoil (on the right) in the stagnation region extracted by the LES. The u'- (a) and the v'-component (b) are made dimensionless by the free-stream velocity, U_∞.

inner porous volume. Specifically, the low pressure spot that corresponds to the region of highest streamline curvature and flow acceleration (at $x/c = 0.17$ in Fig. 10) attracts the surrounding fluid and in particular the boundary layer flow of low momentum, generating an induced flow within the melamine foam. This phenomenon is at the origin of the pronounced momentum deficit of $\overline{u}$ and $\overline{v}$ that is visible in the maps for $x > 0$ and has already been addressed in previous works by the authors [29,30]. Lastly, the effective influence of the porosity on the mean flow field is expected to be less pronounced than the one shown in the maps. This assumption is based on the deviation between experiments and simulations observed in Fig. 11(a) for the porous case.

The velocity fluctuations in the wake of the rod are primarily caused by the shed vortices, which lead to a much larger component in the normal direction than in the streamwise direction. In addition, the porous treatment of the airfoil has a significant effect on the evolution of the turbulent velocity fluctuations as they are convected towards the leading edge. The u' and v' components in the stagnation region are illustrated in Fig. 13(a) and (b) respectively, whereas the values extracted at $y/r_{LE} = 0$ are reported in Fig. 14.

Along the stagnation streamline of the solid airfoil, u' is suppressed due to the no-penetration condition, whereas this reduction is weakened in the porous case. Similarly, the increase of u' experienced on the solid airfoil surface in the surrounding region of the leading edge is mitigated by the presence of porosity. This trend has already been pointed out in Zamponi et al. [29] as a result of the boundary layer characterisation by hot-wire anemometry. Consequently, the main effect of the porous treatment on u' is to dampen the variation of velocity fluctuations near the airfoil.

Moreover, the significant amplification in the upwash component of the velocity fluctuations around the stagnation point that is observed for the solid case is significantly attenuated for the porous one. The reduction in v' is reflected in the Turbulent Kinetic Energy (TKE), reported in Fig. 15, and constitutes a key point in understanding how the porous treatment of the airfoil affects the turbulence distortion. The upwash turbulent velocity is indeed the component that is responsible for the unsteady lift according to the linearised airfoil theory [61] and for the associated noise following Amiet's model [8]. In addition, a second amplification in v' can be observed in the porous case within the inner volume of the melamine foam in proximity to the solid

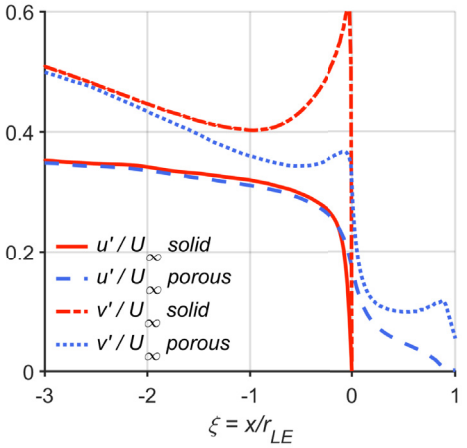

Fig. 14. Turbulence intensity for the solid (red lines) and the porous airfoil (blue lines) extracted by the LES along the stagnation streamline. The u'- and the v'-component are made dimensionless by the free-stream velocity, U_∞. (For interpretation of the references to colour in this figure legend, the reader is referred to the Web version of this article.)

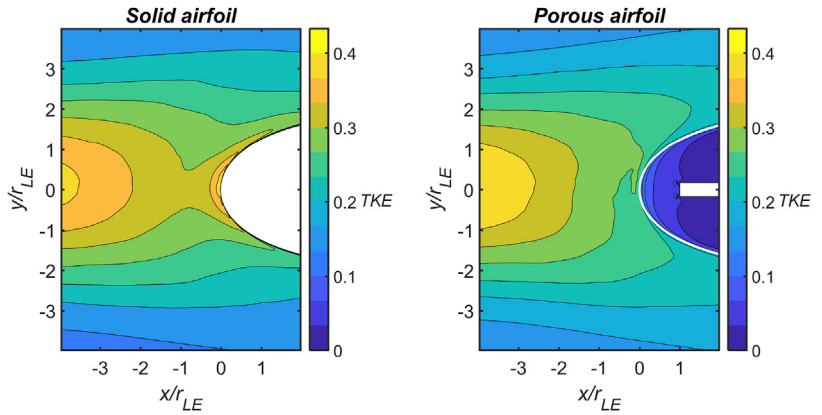

Fig. 15. Turbulent kinetic energy for the solid (on the left) and the porous airfoil (on the right) in the stagnation region extracted by the LES and made dimensionless by the free-stream velocity, U_∞.

center-plane (Fig. 14). The present trend confirms the relevance of the role played by this component on the acoustic field, as already mentioned in Section 3.1.

Finally, the results illustrated in Fig. 11(b) can now be explained through the maps presented in Figs. 12 and 13 and the trends reported in Fig. 14. u' dominates the trend of U' in the upstream flow region where $\alpha \approx 0$. As the stagnation point is being approached, u' is reduced and so is U'. However, since the decrease in $\overline{u}$ is also associated with an increase in α (see Eq. (6)), the contribution of v' to U' becomes more significant in this region. Therefore, the relatively higher U' values in the solid case are caused by the transfer of momentum from the streamwise component to the upwash component of the velocity fluctuations due to the no-penetration condition imposed by the rigid surface. This increase in v' can be detected near the leading edge because the heat transfer of the hot-wire is no longer dominated by the mean flow. Likewise, the absence of the no-penetration condition at the porous surface makes it possible to have a non-zero value for the mean velocity at the stagnation point, which can be considered fictitious in this case. Hence, in the immediate vicinity of the leading edge, α is smaller for the porous airfoil than for the solid one and this yields a further attenuation of U' for the porous case with respect to the solid one.

3.5. Turbulent velocity power spectra

The PSDs of the velocity fluctuations from the experimental data extracted at four specific locations along the stagnation streamline have been computed. The results in Fig. 16 are presented in dB/St with a reference of 1 m^2s^{-2}. The Strouhal number is based on the cylindrical rod diameter and the free-stream velocity.

The measured vortex shedding frequency is found to be at $St = 0.176 \pm 0.001$. This value is slightly lower than what is commonly reported for Reynolds numbers in the high sub-critical regime [62–64]. The discrepancy is most likely caused by

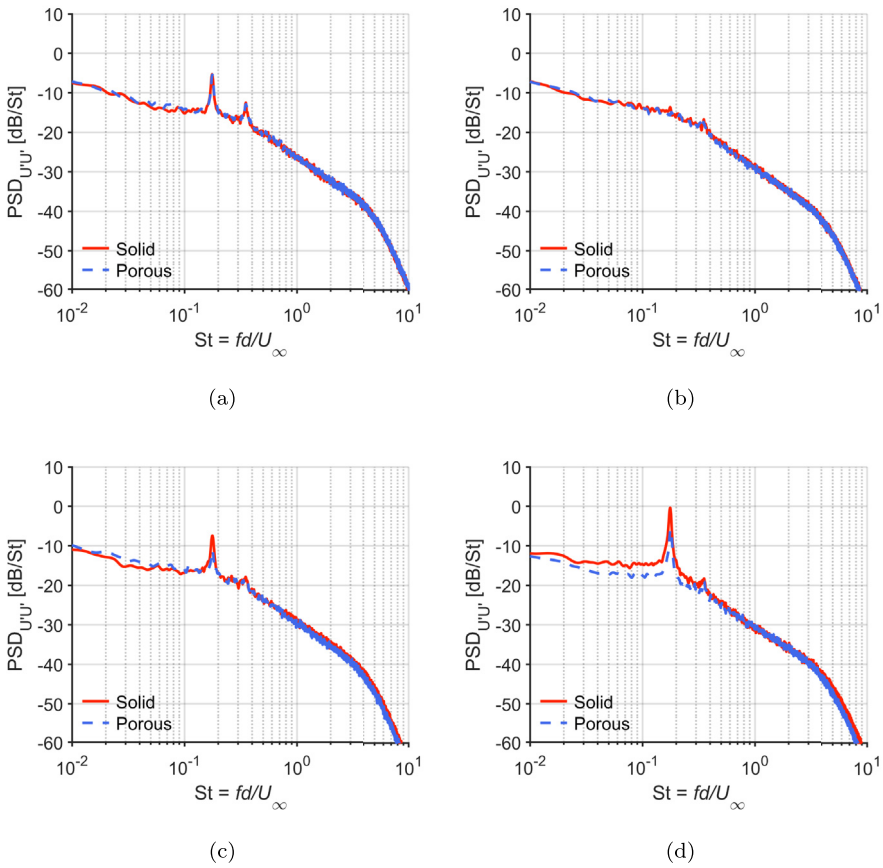

Fig. 16. Velocity fluctuations PSD for the solid (solid red line) and the porous case (dashed blue line) computed from the hot-wire measurements at (a) $\xi = x/r_{LE} = -6.7$, (b) $\xi = -1$, (c) $\xi = -0.5$, and (d) $\xi = -0.05$ with a reference of 1 m^2s^{-2}. (For interpretation of the references to colour in this figure legend, the reader is referred to the Web version of this article.)

the significant blockage of the rod with respect to the wind tunnel width. At $\xi = -6.7$ (Fig. 16(a)), the velocity power spectra clearly present two peaks corresponding to the vortex shedding frequency and its first harmonic. At this position, no difference can be detected between the solid and the porous case, as already observed in Fig. 11(b).

At $\xi = -1$ (Fig. 16(b)), the two considered cases still exhibit the same trend but now the vortex shedding frequency peak turns out to be fully dampened and is no longer visible in the spectra. It has been observed that this peak gradually decreases from the region downstream of the rod up to $\xi = -2$, where it disappears. Interestingly, at this location, the r.m.s. of the velocity fluctuations measured by the hot-wire starts reducing, as shown in Fig. 11(b).

Furthermore, in this intermediate region, the turbulence is not yet distorted and the turbulent fluctuations extracted from the numerical simulations are found to be comparable in the different components, hinting at a local isotropic turbulence. Under this assumption, the size of the largest eddies of the turbulent flow in the streamwise direction can be estimated by evaluating the streamwise integral length scale L_x from the autocorrelation function of the hot-wire time signal and from the local mean flow velocity [65] considering Taylor's frozen turbulence assumption. The resulting $L_x \approx 4.2\, r_{LE}$ will be used in Section 4 to interpret the velocity fluctuation trends by means of the RDT.

At $\xi = -0.8$, the peak at $St = 0.176 \pm 0.001$ reappears for both airfoils and increases in magnitude as the stagnation point is approached. This phenomenon is typical for stagnation-point flows [66] and might be caused by the effect of the flow deceleration that excites the instability associated with the vortex shedding and present in the incoming flow. Indeed, vorticity of sufficiently large scale eddies properly oriented to be stretched can undergo amplification as these structures are convected towards the stagnation region.

Moreover, the solid and porous spectra start diverging from $\xi = -0.5$ (Fig. 11(c)) on, consistently with the U' trends in Fig. 11(b). For the measurement point closest to the airfoil surface at $\xi = -0.05$ (Fig. 16(d)), the part of the power spectrum that is affected by the porosity is the one at low Strouhal numbers, which corresponds to large vortical structures, whereas the high-St region is mostly unaltered.

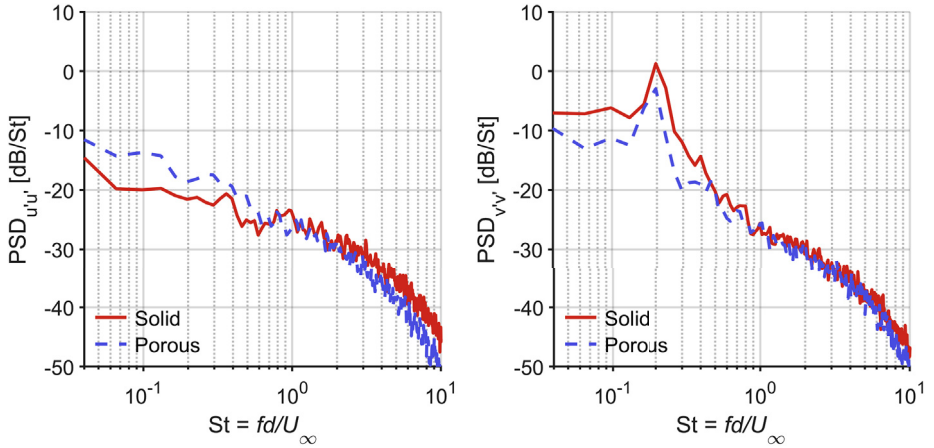

Fig. 17. PSD of the streamwise component (on the left) and the upwash component (on the right) of the velocity fluctuations for the solid (solid red lines) and the porous case (dashed blue lines) extracted by the LES at $\xi = -0.05$. The reference is 1 m^2s^{-2}. (For interpretation of the references to colour in this figure legend, the reader is referred to the Web version of this article.)

Likewise, a better understanding of the turbulence distortion can be gained by the analysis of the LES velocity components separately. Fig. 17 illustrates the PSD of the streamwise ($PSD_{u'u'}$) and the upwash ($PSD_{v'v'}$) component of the velocity fluctuations extracted at $\xi = -0.05$ for the solid and porous configurations. For both components, the porosity mostly alters the power spectrum in the low-St region up to about $St = 0.05$, similarly to the experimental trend. In this range, the limited decrease in u' observed in the stagnation region of the porous airfoil (Fig. 14) is reflected in higher values of $PSD_{u'u'}$ for this configuration with respect to the solid one. Conversely, the power spectra of the upwash component of the velocity fluctuations in the porous case are characterised by lower values of $PSD_{v'v'}$ in the low-St region. The combination of these opposite trends can explain the quantitative difference reported in Fig. 16(d). Furthermore, the porous surface has also an effect on the slope of $PSD_{u'u'}$, as can be deduced by the slightly lower values at high Strouhal numbers. This aspect will be further discussed in Section 4 by means of the RDT.

Finally, the extent of the influence of the porous treatment on the turbulence distortion can be investigated by analysing the power spectra of the velocity fluctuations at several positions around the airfoil leading edge. Fig. 18 reports the PSDs of the two velocity fluctuations components extracted by the LES at three different locations that gradually drift away from the stagnation streamline. Near the leading edge (Fig. 18(a)), $PSD_{u'u'}$ is generally higher in the porous case than in the solid one for the majority of the spectrum, reflecting the trend of u' shown in Fig. 13(b). Interestingly, the vortex shedding peak visible in the power spectrum for the solid airfoil is not present in the one for the porous airfoil. This absence may be linked to a better damping of the vortical structures shed by the rod in the interaction with the porous surface and may clarify why the greatest noise abatement occurs in the one-third octave frequency band containing the vortex shedding peak. In contrast, the trend exhibited by $PSD_{v'v'}$ is closer to the one in Fig. 17. The significant alteration in the PSD of the upwash component of the velocity fluctuations due to the porous treatment is confined to the low-St region, especially for $St < 0.3$. At the intermediate location (Fig. 18(b)), the deviation between the two airfoil configurations is reduced for both velocity components and the power spectra start converging, with the exception of the vortex shedding peak. The present trend is even more pronounced at the location farther from the leading edge (Fig. 18(c)). In conclusion, the porosity is estimated to have an influence on the two components of the velocity fluctuations and, therefore, on the turbulence distortion up to about $\xi = 2$. This result is in agreement with the outcomes of the airfoil boundary layer characterization previously performed [29].

4. Interpretation of the results: Rapid Distortion Theory

The results of the investigation described in Section 3 can be interpreted considering the RDT. Indeed, previous experimental studies [17,67] have demonstrated that, in a region sufficiently close to the stagnation point, the inflow distortion experienced by an airfoil is similar to the one caused by a cylinder that has the same radius as the tangent circle at the airfoil leading edge.

According to Hunt [18], there are two ways in which a bluff body can affect the incident turbulent flow:

- through the distortion of the vorticity field due to potential effect of the body, which alters the mean velocity field around it and upstream of it and leads to a deflection of the streamlines;
- through the pressure exerted by the body, which blocks the turbulence fluctuations by forcing the component of the incident velocity that is normal to its surface to be zero.

The first effect can be considered negligible if the streamwise integral length scale of the turbulent flow is much higher than the characteristic dimension of the body. For the airfoil case, the aforementioned condition can be expressed by $L_x \gg r_{LE}$.

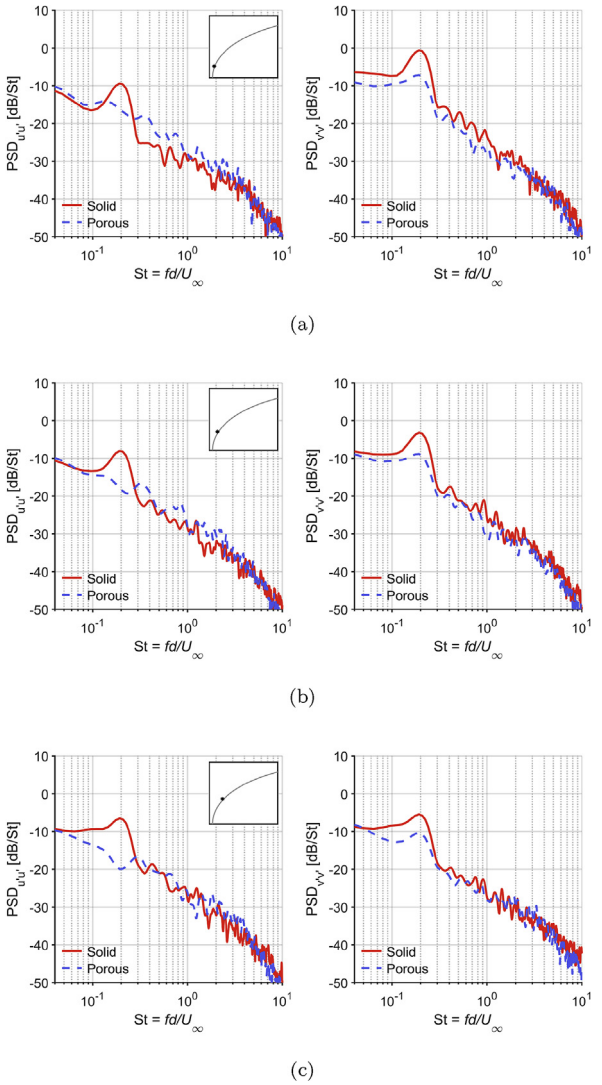

Fig. 18. PSD of the streamwise component (on the left) and the upwash component (on the right) of the velocity fluctuations for the solid (solid red lines) and the porous case (dashed blue lines) extracted by the LES at (a) $x/r_{LE} = 0.04, y/r_{LE} = 0.36$, (b) $x/r_{LE} = 0.15, y/r_{LE} = 0.57$, and (c) $x/r_{LE} = 0.29, y/r_{LE} = 0.78$. The reference is 1 $m^2 s^{-2}$. (For interpretation of the references to colour in this figure legend, the reader is referred to the Web version of this article.)

On the contrary, the body always exerts pressure on the flow, regardless of the ratio between the streamwise integral length scale of the turbulence and the leading-edge radius. The present mechanism is evident for a flat plate, which is characterised by $L_x/r_{LE} \to \infty$. In this extreme case, the vorticity field is almost unaffected by the presence of the body and the only contribution to the alteration of the turbulent velocity fluctuations comes from the second effect.

As showed in Section 3, the turbulence approaching the airfoils at $\xi = -7$ is characterised by $L_x/r_{LE} > 4$. Therefore, it is reasonable to assume that the contribution of the first mechanism is almost negligible. Moreover, a closed-form expression of the RDT for describing the fluctuating velocity field around the body can be derived for the asymptotic case $L_x/r_{LE} \to \infty$ given the mean velocity field and the rate of change of it due to small alterations in the direction of the incident flow [18]. In his theory, Hunt assumes the mean velocity field to be inviscid and the turbulent velocity fluctuations to be small compared with the free-stream velocity. Under these assumptions, an analytical formulation of the r.m.s. of the velocity fluctuations for $L_x/r_{LE} \to \infty$ is [18]

$$\begin{cases} \mathbf{M}_{\mathbf{11}}^{(\mathbf{0})} u'_\infty + \mathbf{M}_{\mathbf{12}}^{(\mathbf{0})} v'_\infty = u' \\ \mathbf{M}_{\mathbf{21}}^{(\mathbf{0})} u'_\infty + \mathbf{M}_{\mathbf{22}}^{(\mathbf{0})} v'_\infty = v' \end{cases} \tag{7}$$

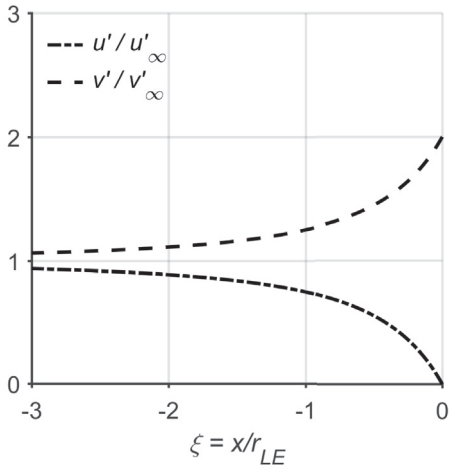

Fig. 19. Trends of the r.m.s. of the velocity fluctuations along the stagnation streamline predicted by the RDT for the asymptotic case $L_x/r_{LE} \to \infty$.

with

$$\mathbf{M}_{ij}^{(0)} = \begin{bmatrix} 1 - \dfrac{(1-\xi)^2 - \upsilon^2}{[(1-\xi)^2 + \upsilon^2]^2} & \dfrac{2(1-\xi)\upsilon}{[(1-\xi)^2 + \upsilon^2]^2} \\ \dfrac{-2(1-\xi)\upsilon}{[(1-\xi)^2 + \upsilon^2]^2} & 1 + \dfrac{(1-\xi)^2 - \upsilon^2}{[(1-\xi)^2 + \upsilon^2]^2} \end{bmatrix}, \tag{8}$$

where $\xi = x/r_{LE} \leq 0$, $\upsilon = y/r_{LE} \leq 0$, and u'_∞ and v'_∞ denote the free-stream values of u' and v' (similarly to the convention adopted for U'_{ref} in Fig. 11(b)). Along the stagnation streamline, Eqs. (7) and (8) yield

$$u' = u'_\infty \left(1 - \frac{1}{(1-\xi)^2}\right), \tag{9}$$

$$v' = v'_\infty \left(1 + \frac{1}{(1-\xi)^2}\right). \tag{10}$$

The trends expressed by Eqs. (9) - (10), valid in the immediate vicinity of the stagnation point, are plotted in Fig. 19. The r.m.s. of the velocity fluctuations in the streamwise direction and the ones in the normal direction are respectively dampened and amplified with reference to their free-stream values. This asymptotic result is in qualitative agreement with what has been observed in Fig. 14 for the solid airfoil and highlights the momentum transfer that occurs between u' and v' due to the no-penetration condition. However, for the porous case, the possibility for part of the incident velocity to penetrate the porous medium alters the mean velocity field around the airfoil and provides a non-zero value for the velocity on the surface. This constitutes a reduced geometrical discontinuity with respect to a solid wall. Hence, the porous body exerts a lower pressure on the turbulence with respect to the solid one and this leads to a damping effect on the variation of the velocity fluctuations starting from $\xi = -0.5$, as discussed in Section 3. Moreover, although the vorticity distortion makes a negligible contribution to the evolution of the velocity fluctuations, it most likely affects the high-St region of the turbulent velocity power spectra, which is associated with small-scale turbulence. Therefore, the deviation in $\text{PSD}_{u'u'}$ between the solid case and the porous one observed in this region (Fig. 17) can be linked to the different way the porosity alters the streamwise velocity fluctuations induced by the vorticity distortion.

In view of the above, the distortion of the large vortical structures that interact with the porous airfoil leading edge is actually attenuated by the penetration of flow within the melamine foam. The present hypothesis is supported by the suppression of the vortex shedding peak that has been observed in the power spectra of the streamwise velocity fluctuations (Fig. 18). Physically, this dampened distortion leads to a decrease in the time variation of the inertia of the incoming turbulent gusts and therefore to a less efficient conversion of their vortical energy into sound.

Finally, the fact that the turbulence is characterised by a large length scale compared to the characteristic dimension of the body implies that the dominant contribution to the incident velocity power spectrum is given by the low-frequency range [18]. This explains why the influence of the porous treatment is visible mostly in this frequency range (Fig. 16(d)), in agreement with the trends of the integrated acoustic power spectra reported in Fig. 9. The aforementioned link confirms the key role played by the attenuation of the distortion of the turbulent eddies in the leading-edge noise reduction mechanism.

5. Conclusion

The present study aims at elucidating the physical mechanisms responsible for the turbulence-interaction noise reduction due to a porous treatment of a thick airfoil. A NACA-0024 profile has been integrated with melamine foam enclosed within a permeable exoskeleton in order to perform a comparison with a solid baseline. The two airfoils have been tested in a rod-airfoil configuration, at a Reynolds number based on the cylindrical rod diameter of $Re_d = 4.1 \times 10^4$.

The focus of the analysis has been put on the stagnation region near the leading edge with the purpose of examining the effect of the porosity on the distortion of the turbulent vortical structures in the interaction with the wing profiles. Specifically, from the acquisition of the mean wall-pressure distributions on their surface, it has been observed that the porous treatment leads to a slight reduction of the flow displacement by the airfoil due to the possibility for the incident velocity to penetrate the inner volume. This phenomenon influences the potential effect of the airfoil and levels out the pressure differences along the surface. However, the C_p deviation between the two cases seems to be limited by the presence of the exoskeleton that preserves the integrity of the NACA-0024 profile's shape.

Furthermore, the flow field along the stagnation streamline has been characterised by means of hot-wire anemometry. The experiments have been compared with LES and showed that the fluctuating velocity field is significantly affected by the porosity when the stagnation region is being approached. In particular, the significant increase of the r.m.s. of the upwash velocity fluctuations experienced by the solid airfoil in the immediate vicinity of the leading edge and predicted by the RDT has not been observed in the porous case, bringing an attenuation of the TKE in the stagnation region. Besides, the analysis of the turbulent velocity power spectra along the stagnation streamline and around the leading edge suggests that the melamine foam has an effect mainly at low frequencies on the large scale structures, with an extent up to about two leading-edge radii from the stagnation point. In addition, the vortex shedding peak in the power spectrum of the streamwise velocity fluctuations close to the airfoil surface has been found to be suppressed due to the porous treatment. Therefore, it can be concluded that the flow penetration through the pores of the melamine foam in the porous airfoil softens the distortion of the largest turbulent eddies by the presence of the body. This evidence is supported by the results of the acoustic beamforming measurements, which indicate that the most appreciable noise abatement is achieved in the one-third octave band containing the tonal component at the shedding frequency, showing a correlation with the attenuation of the turbulent velocity fluctuations.

In summary, the absence of a no-penetration condition on the surface of the porous airfoil reduces the time variation of the vortices' inertia, making the distortion *less rapid*, and eventually leads to a less efficient conversion of vortical energy into sound. This hypothesis for explaining the role of porosity in the turbulence-interaction noise mitigation has been already formed in the past, but, to the authors' knowledge, no experimental evidence of it has ever been provided for a relatively thick airfoil.

CRediT authorship contribution statement

R. Zamponi: Conceptualization, Methodology, Software, Validation, Formal analysis, Investigation, Data curation, Writing - original draft. **S. Satcunanathan:** Methodology, Software, Formal analysis, Data curation, Writing - original draft. **S. Moreau:** Conceptualization, Methodology, Writing - review & editing. **D. Ragni:** Methodology, Supervision, Writing - review & editing. **M. Meinke:** Supervision, Writing - review & editing. **W. Schröder:** Supervision, Writing - review & editing. **C. Schram:** Methodology, Visualization, Supervision, Writing - review & editing, Funding acquisition.

Declaration of competing interest

The authors declare that they have no known competing financial interests or personal relationships that could have appeared to influence the work reported in this paper.

Acknowledgments

This project has received funding from the European Union's Horizon 2020 research and innovation programme under the Marie Skłodowska-Curie grant agreement No. 722401 in the framework of the ITN SmartAnswer. The authors gratefully acknowledge the Gauss Centre for Supercomputing e.V. for funding this project by providing computing time on the GCS Supercomputer HAZEL HEN at Höchstleistungsrechenzentrum Stuttgart. The authors would like also to thank Yves Aurégan from LAUM and Joachim Golliard from CTTM for the help and the support provided in the characterisation of the porous medium parameters.

References

[1] D.B. Hanson, Noise of counter-rotation propellers, J. Aircraft 22 (7) (1985) 609–617, https://doi.org/10.2514/3.45173.
[2] J. Giez, M. Roger, L. Vion, S. Moreau, Effects of intermittency and geometry on the turbulence impingement noise of a CROR Rear-rotor blade, in: 23rd AIAA/CEAS Aeroacoustics Conference, American Institute of Aeronautics and Astronautics, Denver, Colorado, 2017https://doi.org/10.2514/6.2017-3217.
[3] A. Gudel, Acoustique des ventilateurs - Gnration du bruit et moyens de rduction (Acoustics of fans - noise generation and reduction), d. Pyc livres, 1999.
[4] S. Caro, S. Moreau, Aeroacoustic modelling of low pressure axial flow fans, in: 6th Aeroacoustics Conference and Exhibit, American Institute of Aeronautics and Astronautics, Lahaina, HI, U.S.A., 2000https://doi.org/10.2514/6.2000-2094.
[5] S. Perennes, M. Roger, Aerodynamic noise of a two-dimensional wing with high-lift devices, in: 4th AIAA/CEAS Aeroacoustics Conference, American Institute of Aeronautics and Astronautics, Toulouse,France, 1998https://doi.org/10.2514/6.1998-2338.

[6] T.F. Brooks, W.M. Humphreys, Flap-edge aeroacoustic measurements and predictions, J. Sound Vib. 261 (1) (2003) 31–74, https://doi.org/10.1016/S0022-460X(02)00939-2.
[7] M. Roger, C. Schram, L. De Santana, Reduction of airfoil turbulence-impingement noise by means of leading-edge serrations and/or porous material, in: 19th AIAA/CEAS Aeroacoustics Conference, American Institute of Aeronautics and Astronautics, Berlin, Germany, 2013https://doi.org/10.2514/6.2013-2108.
[8] R.K. Amiet, Acoustic radiation from an airfoil in a turbulent stream, J. Sound Vib. 41 (4) (1975) 407–420, https://doi.org/10.1016/S0022-460X(75)80105-2.
[9] R. Paterson, R. Amiet, Acoustic radiation and surface pressure characteristics of an airfoil due to incident turbulence, in: 3rd Aeroacoustics Conference, American Institute of Aeronautics and Astronautics, Palo Alto,CA,U.S.A., 1976https://doi.org/10.2514/6.1976-571.
[10] W. Olsen, J. Wagner, Effect of thickness on airfoil surface noise, AIAA J. 20 (3) (1982) 437–439, https://doi.org/10.2514/3.7922.
[11] S. Oerlemans, P. Migliore, Aeroacoustic wind tunnel tests of wind turbine airfoils, in: 10th AIAA/CEAS Aeroacoustics Conference, American Institute of Aeronautics and Astronautics, Manchester, UK, 2004https://doi.org/10.2514/6.2004-3042.
[12] S. Moreau, M. Roger, Effect of angle of attack and airfoil shape on turbulence-interaction noise, in: 11th AIAA/CEAS Aeroacoustics Conference, American Institute of Aeronautics and Astronautics, Monterey, California, 2005https://doi.org/10.2514/6.2005-2973.
[13] W.J. Devenport, J.K. Staubs, S.A. Glegg, Sound radiation from real airfoils in turbulence, J. Sound Vib. 329 (17) (2010) 3470–3483, https://doi.org/10.1016/j.jsv.2010.02.022.
[14] J. Gill, X. Zhang, P. Joseph, Symmetric airfoil geometry effects on leading edge noise, J. Acoust. Soc. Am. 134 (4) (2013) 2669–2680, https://doi.org/10.1121/1.4818769.
[15] D. Kim, G.-S. Lee, C. Cheong, Inflow broadband noise from an isolated symmetric airfoil interacting with incident turbulence, J. Fluid Struct. 55 (2015) 428–450, https://doi.org/10.1016/j.jfluidstructs.2015.03.015.
[16] J. Christophe, Application of Hybrid Methods to High Frequency Aeroacoustics, Ph.D. thesis, Universit Libre de Bruxelles, Nov. 2011.
[17] L.D. Santana, J. Christophe, C. Schram, W. Desmet, A Rapid Distortion Theory modified turbulence spectra for semi-analytical airfoil noise prediction, J. Sound Vib. 383 (2016) 349–363, https://doi.org/10.1016/j.jsv.2016.07.026.
[18] J.C.R. Hunt, A theory of turbulent flow round two-dimensional bluff bodies, J. Fluid Mech. 61 (4) (1973) 625–706, https://doi.org/10.1017/S0022112073000893.
[19] G.K. Batchelor, I. Proudman, The effect of rapid distortion of a fluid in turbulent motion, Q. J. Mech. Appl. Math. 7 (1) (1954) 83–103, https://doi.org/10.1093/qjmam/7.1.83.
[20] S. Lee, Reduction of blade-vortex interaction noise through porous leading edge, AIAA J. 32 (3) (1994) 480–488, https://doi.org/10.2514/3.12011.
[21] M. Roger, S. Moreau, Airfoil turbulence-impingement noise reduction by porosity or wavy leading-edge cut: experimental investigations, in: 45th International Congress and Exposition on Noise Control Engineering, INTER-NOISE, Hamburg, Germany, 2016, p. 10.
[22] T. Geyer, E. Sarradj, J. Giesler, M. Hobracht, Experimental assessment of the noise generated at the leading edge of porous airfoils using microphone array techniques, in: 17th AIAA/CEAS Aeroacoustics Conference (32nd AIAA Aeroacoustics Conference), American Institute of Aeronautics and Astronautics, Portland, Oregon, 2011https://doi.org/10.2514/6.2011-2713.
[23] T. Geyer, E. Sarradj, J. Giesler, Application of a beamforming technique to the measurement of airfoil leading edge noise, Adv. Acoust. Vibr. (2012), https://doi.org/10.1155/2012/905461.
[24] E. Sarradj, T. Geyer, Symbolic regression modeling of noise generation at porous airfoils, J. Sound Vib. 333 (14) (2014) 3189–3202, https://doi.org/10.1016/j.jsv.2014.02.037.
[25] T.F. Geyer, A. Lucius, M. Schrdter, M. Schneider, E. Sarradj, Reduction of turbulence interaction noise through airfoils with perforated leading edges, Acta Acustica united Acustica 105 (1) (2019) 109–122, https://doi.org/10.3813/AAA.919292.
[26] F. Avallone, D. Casalino, D. Ragni, Impingement of a propeller-slipstream on a leading edge with a flow-permeable insert: a computational aeroacoustic study, Int. J. Aeroacoustics 17 (68) (2018) 687–711, https://doi.org/10.1177/1475472X18788961.
[27] T. Sinnige, B.D. Corte, R. De Vries, F. Avallone, R. Merino-Martnez, D. Ragni, G. Eitelberg, L.L.M. Veldhuis, Alleviation of propeller-slipstream-induced unsteady pylon loading by a flow-permeable leading edge, J. Aircraft 56 (3) (2019) 1214–1230, https://doi.org/10.2514/1.C035250.
[28] M. Kuczmarski, J. Johnston, Acoustic Absorption in Porous Materials, Technical Report NASA/TM-2011-216995, NASA Glenn Research Center, 2011.
[29] R. Zamponi, D. Ragni, N. Van de Wyer, C. Schram, Experimental investigation of airfoil turbulence-impingement noise reduction using porous treatment, in: 25th AIAA/CEAS Aeroacoustics Conference, American Institute of Aeronautics and Astronautics, Delft, The Netherlands, 2019https://doi.org/10.2514/6.2019-2649.
[30] S. Satcunanathan, M.H. Meinke, W. Schrder, Prediction of noise mitigation by porous media based on a direct-hybrid CFD/CAA method, in: 25th AIAA/CEAS Aeroacoustics Conference, American Institute of Aeronautics and Astronautics, Delft, The Netherlands, 2019https://doi.org/10.2514/6.2019-2696.
[31] M.C. Jacob, J. Boudet, D. Casalino, M. Michard, A rod-airfoil experiment as a benchmark for broadband noise modeling, Theor. Comput. Fluid Dynam. 19 (3) (2005) 171–196, https://doi.org/10.1007/s00162-004-0108-6.
[32] V. Lorenzoni, M. Tuinstra, F. Scarano, On the use of time-resolved particle image velocimetry for the investigation of rodairfoil aeroacoustics, J. Sound Vib. 331 (23) (2012) 5012–5027, https://doi.org/10.1016/j.jsv.2012.05.034.
[33] L.D. de Santana, Semi-analytical Methodologies for Airfoil Noise Prediction, Ph.D. thesis, KU Leuven, Jun. 2015.
[34] W.J. Devenport, R.L. Simpson, M.B. Dewitz, N.K. Agarwal, Effects of a leading-edge fillet on the flow past an appendage-body junction, AIAA J. 30 (9) (1992) 2177–2183, https://doi.org/10.2514/3.11201.
[35] D.L. Johnson, J. Koplik, R. Dashen, Theory of dynamic permeability and tortuosity in fluid-saturated porous media, J. Fluid Mech. 176 (-1) (1987) 379, https://doi.org/10.1017/S0022112087000727.
[36] Y. Champoux, J. Allard, Dynamic tortuosity and bulk modulus in air-saturated porous media, J. Appl. Phys. 70 (4) (1991) 1975–1979, https://doi.org/10.1063/1.349482.
[37] D. Lafarge, P. Lemarinier, J.F. Allard, V. Tarnow, Dynamic compressibility of air in porous structures at audible frequencies, J. Acoust. Soc. Am. 102 (4) (1997) 1995–2006, https://doi.org/10.1121/1.419690.
[38] M. Niskanen, J.-P. Groby, A. Duclos, O. Dazel, J.C. Le Roux, N. Poulain, T. Huttunen, T. Lhivaara, Deterministic and statistical characterization of rigid frame porous materials from impedance tube measurements, J. Acoust. Soc. Am. 142 (4) (2017) 2407–2418, https://doi.org/10.1121/1.5008742.
[39] H. H. Bruun, Hot-wire anemometry: principles and signal analysis, Meas. Sci. Technol. 7 (10). doi:10.1088/0957-0233/7/10/024.
[40] P. Welch, The use of fast Fourier transform for the estimation of power spectra: a method based on time averaging over short, modified periodograms, IEEE Trans. Audio Electroacoust. 15 (2) (1967) 70–73, https://doi.org/10.1109/TAU.1967.1161901.
[41] R. P. Dougherty, Spiral-shaped array for broadband imaging, Pat. US 5,838,284 (1998).
[42] R. Zamponi, N.V. de Wyer, C. Schram, An improved Regularization of the generalized inverse beamforming applied to a benchmark database, in: 7th Berlin Beamforming Conference, BeBeC, Berlin, Germany, 2018.
[43] R. Zamponi, N. Van de Wyer, C. Schram, Benchmark assessment of an improved Regularization technique for generalized inverse beamforming, in: 2018 AIAA/CEAS Aeroacoustics Conference, American Institute of Aeronautics and Astronautics, Atlanta, Georgia, 2018https://doi.org/10.2514/6.2018-4106.
[44] R. Merino-Martnez, P. Sijtsma, A.R. Carpio, R. Zamponi, S. Luesutthiviboon, A.M. Malgoezar, M. Snellen, C. Schram, D.G. Simons, Integration methods for distributed sound sources, Int. J. Aeroacoustics 18 (45) (2019) 444–469, https://doi.org/10.1177/1475472X19852945.
[45] R. Merino-Martnez, S. Luesutthiviboon, R. Zamponi, A. Rubio Carpio, D. Ragni, P. Sijtsma, M. Snellen, C. Schram, Assessment of the accuracy of microphone array methods for aeroacoustic measurements, J. Sound Vib. 470 (2020) 115176, https://doi.org/10.1016/j.jsv.2020.115176.
[46] P. Sijtsma, Phased Array Beamforming Applied to Wind Tunnel and Fly-Over Tests, Tech. rep., National Aerospace Laboratory NLR, Oct. 2010.
[47] C.J. Bahr, W.C. Horne, Advanced background subtraction applied to aeroacoustic wind tunnel testing, in: 21st AIAA/CEAS Aeroacoustics Conference, American Institute of Aeronautics and Astronautics, Dallas, TX, 2015https://doi.org/10.2514/6.2015-3272.
[48] T. Suzuki, L1 generalized inverse beam-forming algorithm resolving coherent/incoherent, distributed and multipole sources, J. Sound Vib. 330 (24) (2011) 5835–5851, https://doi.org/10.1016/j.jsv.2011.05.021.

[49] R. Zamponi, P. Chiariotti, G. Battista, C. Schram, P. Castellini, 3D Generalized Inverse Beamforming in wind tunnel aeroacoustic testing: application to a Counter Rotating Open Rotor aircraft model, Appl. Acoust. 163 (2020) 107229, https://doi.org/10.1016/j.apacoust.2020.107229.
[50] A. Rubio Carpio, R. Merino Martnez, F. Avallone, D. Ragni, M. Snellen, S. van der Zwaag, Experimental characterization of the turbulent boundary layer over a porous trailing edge for noise abatement, J. Sound Vib. 443 (2019) 537–558, https://doi.org/10.1016/j.jsv.2018.12.010.
[51] S. Whitaker, The Method of Volume Averaging, Vol. 13 of Theory and Applications of Transport in Porous Media, Springer Netherlands, Dordrecht, 1999https://doi.org/10.1007/978-94-017-3389-2.
[52] S. Satcunathan, R. Zamponi, M. Meinke, N. Van de Wyer, C. Schram, W. Schrder, Validation of a model for acoustic absorption in porous media, in: 48th International Congress and Exhibition on Noise Control Engineering, INTER-NOISE, Madrid, Spain, 2019.
[53] L. Schneiders, D. Hartmann, M. Meinke, W. Schrder, An accurate moving boundary formulation in cut-cell methods, J. Comput. Phys. 235 (2013) 786–809 doi:0.1016/j.jcp.2012.09.038.
[54] P. Batten, U. Goldberg, S. Chakravarthy, Interfacing statistical turbulence closures with large-eddy simulation, AIAA J. 42 (3) (2004) 485–492, https://doi.org/10.2514/1.3496.
[55] M.J. Priddin, C.C. Paruchuri, P. Joseph, L.J. Ayton, A semi-analytic and experimental study of porous leading edges, in: 25th AIAA/CEAS Aeroacoustics Conference, American Institute of Aeronautics and Astronautics, Delft, The Netherlands, 2019https://doi.org/10.2514/6.2019-2552.
[56] E. Sarradj, T. Geyer, Noise generation by porous airfoils, in: 13th AIAA/CEAS Aeroacoustics Conference (28th AIAA Aeroacoustics Conference), American Institute of Aeronautics and Astronautics, Rome, Italy, 2007https://doi.org/10.2514/6.2007-3719.
[57] T. Geyer, E. Sarradj, C. Fritzsche, Measurement of the noise generation at the trailing edge of porous airfoils, Exp. Fluid 48 (2) (2010) 291–308, https://doi.org/10.1007/s00348-009-0739-x.
[58] J.-D. Vagt, Hot-wire probes in low speed flow, Prog. Aero. Sci. 18 (1979) 271–323, https://doi.org/10.1016/0376-0421(77)90010-0.
[59] P.W. Bearman, Some measurements of the distortion of turbulence approaching a two-dimensional bluff body, J. Fluid Mech. 53 (3) (1972) 451, https://doi.org/10.1017/S0022112072000254.
[60] R.E. Britter, J.C.R. Hunt, J.C. Mumford, The distortion of turbulence by a circular cylinder, J. Fluid Mech. 92 (2) (1979) 269, https://doi.org/10.1017/S0022112079000628.
[61] M.E. Goldstein, H. Atassi, A complete second-order theory for the unsteady flow about an airfoil due to a periodic gust, J. Fluid Mech. 74 (4) (1976) 741–765, https://doi.org/10.1017/S0022112076002036.
[62] E. Achenbach, Vortex shedding from spheres, J. Fluid Mech. 62 (2) (1974) 209–221, https://doi.org/10.1017/S0022112074000644.
[63] J.-C. Giret, A. Sengissen, S. Moreau, M. Sanjose, J.-C. Jouhaud, Noise source analysis of a rodairfoil configuration using unstructured large-eddy simulation, AIAA J. 53 (4) (2015) 1062–1077, https://doi.org/10.2514/1.J053371.
[64] C. Zhang, M. Sanjose, S. Moreau, Turbulent flow and noise sources on a circular cylinder in the critical regime, 085009, Advances 9 (2019) 1–16, https://doi.org/10.1063/1.5121544.
[65] N.V.C. Swamy, B.H.L. Gowda, V.R. Lakshminath, Auto-correlation measurements and integral time scales in three-dimensional turbulent boundary layers, Appl. Sci. Res. 35 (4) (1979) 237–249, https://doi.org/10.1007/BF00418215.
[66] S.P. Sutera, P.F. Maeder, J. Kestin, On the sensitivity of heat transfer in the stagnation-point boundary layer to free-stream vorticity, J. Fluid Mech. 16 (4) (1963) 497–520, https://doi.org/10.1017/S0022112063000963.
[67] P.F. Mish, W.J. Devenport, An experimental investigation of unsteady surface pressure on an airfoil in turbulencePart 2: sources and prediction of mean loading effects, J. Sound Vib. 296 (3) (2006) 447–460, https://doi.org/10.1016/j.jsv.2005.08.009.